



HAL
open science

Preindustrial control simulations with HadGEM3-GC3.1 for CMIP6

Matthew B Menary, Till Kuhlbrodt, Jeff Ridley, Martin Andrews, Oscar Dimdore-miles, Julie Deshayes, Rosie Eade, Lesley Gray, Sarah Ineson, Juliette Mignot, et al.

► To cite this version:

Matthew B Menary, Till Kuhlbrodt, Jeff Ridley, Martin Andrews, Oscar Dimdore-miles, et al.. Preindustrial control simulations with HadGEM3-GC3.1 for CMIP6. *Journal of Advances in Modeling Earth Systems*, 2018, 10 (12), pp.3049-3075. 10.1029/2018MS001495 . hal-02190743

HAL Id: hal-02190743

<https://hal.science/hal-02190743>

Submitted on 2 Sep 2021

HAL is a multi-disciplinary open access archive for the deposit and dissemination of scientific research documents, whether they are published or not. The documents may come from teaching and research institutions in France or abroad, or from public or private research centers.

L'archive ouverte pluridisciplinaire **HAL**, est destinée au dépôt et à la diffusion de documents scientifiques de niveau recherche, publiés ou non, émanant des établissements d'enseignement et de recherche français ou étrangers, des laboratoires publics ou privés.



Distributed under a Creative Commons Attribution - NonCommercial - ShareAlike 4.0 International License

RESEARCH ARTICLE

10.1029/2018MS001495

Special Section:

The UK Earth System Models for CMIP6

Key Points:

- Preindustrial control simulations for CMIP6 with HadGEM3-GC3.1 are presented using two model resolutions
- Our evaluation focuses on interannual variability in key climate indices
- The high-resolution model shows improvements in ENSO, AMV, and in the depth structure of the AMOC. However, the ACC strength is worse

Correspondence to:

M. B. Menary,
matthew.menary@locean-ipsl.upmc.fr

Citation:

Menary, M. B., Kuhlbrodt, T., Ridley, J., Andrews, M. B., Dimdore-Miles, O. B., Deshayes, J., et al. (2018). Preindustrial control simulations with HadGEM3-GC3.1 for CMIP6. *Journal of Advances in Modeling Earth Systems*, 10, 3049–3075. <https://doi.org/10.1029/2018MS001495>

Received 3 SEP 2018

Accepted 16 NOV 2018

Accepted article online 22 NOV 2018

Published online 13 DEC 2018

©2018 Crown copyright. This article is published with the permission of the Controller of HMSO and the Queen's Printer for Scotland.

This is an open access article under the terms of the Creative Commons Attribution-NonCommercial-NoDerivs License, which permits use and distribution in any medium, provided the original work is properly cited, the use is non-commercial and no modifications or adaptations are made.

Preindustrial Control Simulations With HadGEM3-GC3.1 for CMIP6

Matthew B. Menary^{1,2} , Till Kuhlbrodt³ , Jeff Ridley¹ , Martin B. Andrews¹ , Oscar B. Dimdore-Miles⁴ , Julie Deshayes² , Rosie Eade¹ , Lesley Gray⁴, Sarah Ineson¹, Juliette Mignot² , Christopher D. Roberts^{1,5} , Jon Robson³ , Richard A. Wood¹ , and Prince Xavier¹ 

¹Met Office Hadley Centre, Met Office, Exeter, UK, ²LOCEAN/IPSL, Sorbonne Universités (SU)-CNRS-IRD-MNHN, Paris, France, ³NCAS, Department of Meteorology, University of Reading, Reading, UK, ⁴NCAS, Department of Physics, University of Oxford, Oxford, UK, ⁵European Centre for Medium-Range Weather Forecasts, Reading, UK

Abstract Preindustrial control simulations with the third Hadley Centre Global Environmental Model, run in the Global Coupled configuration 3.1 of the Met Office Unified Model (HadGEM3-GC3.1) are presented at two resolutions. These are N216ORCA025, which has a horizontal resolution of 60 km in the atmosphere and 0.25° in the ocean, and N96ORCA1, which has a horizontal resolution of 130 km in the atmosphere and 1° in the ocean. The aim of this study is to document the climate variability in these simulations, make comparisons against present-day observations (albeit under different forcing), and discuss differences arising due to resolution. In terms of interannual variability in the leading modes of climate variability the two resolutions behave generally very similarly. Notable differences are in the westward extent of El Niño and the pattern of Atlantic multidecadal variability, in which N216ORCA025 compares more favorably to observations, and in the Antarctic Circumpolar Current, which is far too weak in N216ORCA025. In the North Atlantic region, N216ORCA025 has a stronger and deeper Atlantic Meridional Overturning Circulation, which compares well against observations, and reduced biases in temperature and salinity in the North Atlantic subpolar gyre. These simulations are being provided to the sixth Coupled Model Intercomparison Project (CMIP6) and provide a baseline against which further forced experiments may be assessed.

Plain Language Summary In this paper, we present the latest computer models of the joint atmosphere and ocean system. These models were developed at the U.K. Met Office Hadley Centre. They are designed to simulate the climate of the past, present, and future and to be used in scientific analysis and decision making. In this study, they are intended to simulate a continuous *preindustrial* state, to provide a reference level for future experiments and analysis. We present two resolutions of the same model, where the resolution is analogous to the number of pixels on, for example, a smartphone display. We find that the model with greater resolution also simulates many aspects of the global climate better than the model with lower resolution. These include El Niño, sea surface temperature variability in the Atlantic Ocean, and the depth of the AMOC in the North Atlantic. However, in other aspects, such as the strength of the major current circling Antarctica, this version is worse.

1. Introduction

As part of the sixth coupled model intercomparison project (CMIP6, Eyring et al., 2016), geoscience institutions across the world have been constructing and running coupled climate models to be submitted to a vast online and free-to-access database. In order for institutes to participate in this project, they are required to run a set of baseline simulations, denoted the Diagnostic, Evaluation and Characterization of Klima. These consist of four experiments: a coupled control simulation with preindustrial forcings (piControl), an atmosphere-only simulation with prescribed sea ice and sea surface temperatures (AMIP), a coupled control simulation with an abrupt increase in carbon dioxide forcing (CO₂) to four times preindustrial (abrupt4xCO₂), and a coupled simulation in which preindustrial forcing increases by 1% per year (1 pctCO₂). In addition, they must also complete a simulation with historical forcings since 1850.

In this paper, we document the setup and performance of the piControl simulation with two resolutions of the U.K. climate model for CMIP6 (described next) and discuss the potential effects of resolution. The piControl

simulations provide both a baseline against which forced experiments can be assessed and insight into the mechanisms of unforced variability (Eyring et al., 2016)—some modes of which we specifically analyze here. In addition, we compare two versions of the model at different resolutions, as model resolution may impact the representation of important processes. For example, the horizontal resolution of atmosphere and/or ocean submodels in coupled climate models has been shown to be important for both the mean state of the North Atlantic Ocean (Menary et al., 2015; Mignot et al., 2013) and the behavior of the Atlantic Meridional Overturning Circulation (AMOC), both in terms of internal decadal variability (Bryan et al., 2006; Hodson & Sutton, 2012) and its response to climate change (Roberts et al., 2004). Related to the ocean resolution, higher-resolution topography may be important in setting the pathways of deep water advection (Spence et al., 2011) and wave dynamics (Roussenov et al., 2008). At higher ocean resolution, eddy-induced mixing can begin to be resolved rather than parameterized and improvements in sea surface temperature (SST) gradients allowed by increased ocean resolution can lead directly to improved atmospheric responses (Minobe et al., 2008).

In the atmosphere, increased horizontal resolution is associated with increased ocean-to-land moisture transport (Demory et al., 2014) and improved surface temperature biases in the major oceanic upwelling regions (Gent et al., 2010). In addition, increased atmospheric resolution has been linked with improvements in the North Atlantic storm tracks and North Atlantic Oscillation (NAO; Marti et al., 2010) although these may also be linked to oceanic resolution (Scaife et al., 2011).

1.1. HadGEM3-GC3.1

The third Hadley Centre Global Environmental Model, run in the Global Coupled configuration 3.1 of the Met Office Unified Model (HadGEM3-GC3.1), represents the latest climate model from the U.K. Met Office. The development of the underlying physical climate model is documented in Williams et al. (2018). In that study, the model was forced with external forcings appropriate for the year 2000 and the overall mean state of the model described. Kuhlbrodt et al. (2018) describe the low-resolution version of this model as will be used for the U.K. Earth System Model (constructed in collaboration with the U.K. academic community) within CMIP6. That comparison mostly presents simulations again forced with year 2000 forcings. Here we present both the high- and low-resolution versions of the model forced with the CMIP6-specified preindustrial forcings and investigate aspects of the variability. In this analysis, when comparing with observations of the variability of the present day/recent past, we acknowledge that there is additional uncertainty due to the implicit assumption that the nature of variability has remained unchanged, which may not always be the case (Schär et al., 2004). For each climate index that we present, the possible uncertainty arising from our use of present-day observations is discussed.

The two resolutions of HadGEM3-GC3.1 are denoted N216ORCA025 and N96ORCA1 and couple the Unified Model atmosphere model (Walters et al., 2017) and Nucleus for European Modelling of the Ocean ocean model (Madec, 2008). In N216ORCA025, the atmospheric resolution is approximately 60 km and the ocean resolution is 0.25° , with coupling every hour, as detailed in Williams et al. (2018). In N96ORCA1, the atmospheric resolution is approximately 135 km and the ocean resolution is 1° (with refinement to 0.33° within 15° north or south of the equator), with coupling every 3 hr, as detailed in Kuhlbrodt et al. (2018). The vertical resolution in the atmosphere and ocean is the same in both setups, with 85 pressure levels in the atmosphere and 75 depth levels in the ocean. Both models use the JULES land surface (Walters et al., 2017) and CICE sea ice (Ridley et al., 2018) models at their atmospheric and ocean resolutions, respectively. See Kuhlbrodt et al. (2018) for a list of the associated ocean/sea ice parameter differences between the two resolutions. At the 1° ocean resolution in N96ORCA1, a parameterization for eddy-induced transports is required (Kuhlbrodt et al., 2018), which uses a globally uniform coefficient. How to implement such a parameterization at 0.25° ocean resolution is under debate, and in N216ORCA025 such a parameterization is not used. In the atmosphere, there are a limited set of parameter differences, as detailed in Kuhlbrodt et al. (2018, their Table 1).

1.2. Initialization and Run Length

In this analysis we use 500 model years of the N96ORCA1 piControl simulation and 300 years of the N216ORCA025 piControl simulation. At the high resolution of N216ORCA025, the simulation runs at approximately 1.4 model years per real day using 4,320 cores. For comparison, N96ORCA1 completes approximately 2.3 years per day on 416 cores.

The N96ORCA1 and N216ORCA025 piControl runs differ in both their run length and in the prior spin-up process. The spin-up integrations in both cases were run entirely in synchronously coupled mode (i.e., simply a continuous run of the full coupled model from a given initial state). CMIP6 preindustrial forcings were used

Table 1
Greenhouse Gases Applied in the Preindustrial Control Simulations

Greenhouse gas	Concentration	Mass mixing ratio (kg/kg)
CO ₂	284.317 ppm ^a	4.3182×10^{-4}
CH ₄	808.25 ppb ^b	4.4640×10^{-7}
N ₂ O	273.02 ppb	4.1466×10^{-7}
CFC-12 equivalent	16.51 ppt ^c	6.8996×10^{-11}
HFC-134a equivalent	19.15 ppt	6.7456×10^{-11}

Note. CFC = chlorofluorocarbon; HFC = hydrofluorocarbon.

^appm: parts per million. ^bppb: parts per billion. ^cppt: parts per trillion.

throughout the spin-up and piControl phases, except that only preliminary versions of some of the forcings were available for the early stages of the spin-up runs. Since the sole purpose of the spin-up phase is to bring the model acceptably close to an equilibrium, the details of the spin-up phase are not considered critical to the behavior of the piControl which is the focus of this paper. At the designated end of the spin-up period the run was simply continued, with this point being designated the start of the piControl run. Some global measures of the disequilibrium of the piControl runs are discussed in section 2.

For N96ORCA1 the ocean initial conditions for the spin-up were the mean of the years 1950–1954 from the EN4 ocean analysis (Good et al., 2013). N96ORCA1 was subsequently spun-up for 652 model years, and this state was deemed the starting point of the piControl simulation.

For N216ORCA025 the initial conditions were taken from year 100 of a run with fixed present-day forcings, preliminary to that reported in Williams et al. (2018). After 50 model years, a bug was found and fixed that had the effect of cooling the global climate. Within a further 50 years, the surface air temperature had recovered and was approaching its final, spun-up value (section 2). In total, the N216ORCA025 simulation was spun-up for 353 model years, after which the model was deemed to be sufficiently equilibrated to designate the start of the piControl (see discussion of piControl trends in section 2).

1.3. Preindustrial Forcings

The preindustrial CMIP6 forcings constitute interannually invariant forcings appropriate for the year 1850. These are well-mixed greenhouse gases (including CO₂), ozone, solar, tropospheric aerosol, and stratospheric volcanic aerosol. In addition, the land surface is prescribed with land use tiles appropriate for 1850. These forcings will be described in detail in a parallel publication, and so we only briefly summarize them next.

The greenhouse gases provided by CMIP6 (Meinshausen et al., 2017) include variations with latitude although in our implementation they remain globally well mixed and are input as global, annual means. Instead of setting all the individual chlorofluorocarbon and hydrofluorocarbon species separately, effective chlorofluorocarbon and hydrofluorocarbon concentrations are used. The specific concentrations are shown in Table 1. Ozone is prescribed as a three-dimensional field, where previously we had only prescribed it as a zonal mean field (Williams et al., 2015). The solar forcing is constructed from time-averaged historical data for the period 1850–1873, which covers solar cycles 9 and 10 (as counted from the year 1755).

The climate model requires primary emissions of black carbon and organic carbon aerosol, as well as gas phase emissions of sulfur dioxide (SO₂), dimethylsulfide and monoterpene, which are oxidized to sulfate aerosol. Black carbon, organic carbon, and SO₂ are included from both biomass and anthropogenic sources, at values appropriate for the year 1850. These emissions are provided as external forcing files to the UKCA GLOMAP-mode aerosol scheme (Mann et al., 2010).

For the stratospheric volcanic aerosol forcing, the piControl simulation uses the long-term mean from the historical period 1850–2014, including the seasonal cycle. This time series was itself first constructed using a combination of satellite products and model simulations. The climate model subsequently reads in the spectral properties of these stratospheric aerosol directly into the radiation scheme, bypassing the aerosol scheme used for tropospheric aerosol. The model is provided with aerosol extinction, absorption, and asymmetry parameters in both the shortwave and longwave.

Finally, the climate model requires external specification of nine land surface types: urban, bare soil, lake, land ice, and five plant functional types. The plant functional types are C3 and C4 grasses, needleleaf and broadleaf

Table 2
Mean and Trends (per Century) in Global Mean Measures of Climate Equilibrium

Variable	N216ORCA025			N96ORCA1	
	Unit	Mean	Trend	Mean	Trend
TOA ^a	W/m ²	0.314	−0.001	0.196	−0.002
SAT ^b	°C	14.96	0.11	14.76	0.03
OceTemp ^c	°C	3.962	0.074	4.007	0.035
OceSal ^d	PSU	34.7290	−0.0001	37.7220	0.0001

Note. Significant trends at 95% level in bold.

^aTOA: Net radiative balance at top of atmosphere. ^bSAT: surface air temperature.

^cOceTemp: full depth ocean temperature. ^dOceSal: full depth ocean salinity.

trees, and shrubs (Essery et al., 2003). These are not directly supplied by CMIP6 and so a conversion from crop and pasture fraction (supplied by CMIP6) is undertaken.

In this paper, we aim to document the piControl simulations with two resolutions of HadGEM3-GC3.1. This will provide a baseline against which historical, scenario, and other simulations with these models can be compared. In order to do this, we show and describe a set of key climate phenomena. Further work will be undertaken during CMIP6 to investigate each of these phenomena individually. It is important to begin to understand this unforced variability as any response to external forcings in future experiments with these models will either exist on top of or interact with this variability.

2. Key Measures of Climate Variability

Before investigating the interannual variability in some key climate phenomena, we provide a global context with measures of the global energy/water balance of the simulated climate system (Table 2). The centennial trends in net top of atmosphere (TOA) radiation in both resolutions are indistinguishable from zero. Both resolutions show a positive mean TOA, which would be expected to equilibrate to zero only on a timescale of many centuries, while surface temperature equilibrates fairly quickly (Geoffroy et al., 2013). Radiative forcing from well-mixed greenhouse gases in 1850 has been estimated at several tenths of a W m^{−2} (relative to 1750), although aerosol effects likely acted to reduce the total forcing (Eyring et al., 2016; Myrhe et al., 2013). The positive TOA heat flux is reflected in warming trends in global ocean temperature/heat content, dominated by a gradual warming of the deep ocean (not shown), while the surface air temperature is close to stable in both simulations. The full depth ocean salinity is relatively stable, suggesting that the global freshwater processes in the model are well equilibrated.

In the remainder of this section we introduce some key measures of the climate system, relevant for discussions of interannual climate variability. These are the El Niño–Southern Oscillation (ENSO; section 2.1), the NAO (section 2.2), Tropical Intraseasonal Variability including the Madden-Julian Oscillation (MJO; section 2.3), Atlantic Multidecadal Variability (AMV, sometimes also called the Atlantic Multidecadal Oscillation; section 2.4), stratospheric variability including the Quasi-Biennial Oscillation (QBO; section 2.5), the Antarctic Circumpolar Current (ACC; section 2.6), the AMOC at 26.5°N (section 2.7), and the North Atlantic subpolar gyre (NA SPG; section 2.8).

An uncertainty arises when comparing model preindustrial control integrations with observations that are typically from a more recent period. This is a particular issue when the two model resolutions differ, and we compare with observations to evaluate whether one solution is better than the other. In each of these cases we have examined the difference between the preindustrial control (this paper) and the *present-day* control (Williams et al., 2018) of the N216ORCA015 model. In each case we find that the difference due to the differing time periods is less than the difference between the two model resolutions with preindustrial forcing, confirming that it makes sense to evaluate the piControl models against present-day observations.

2.1. ENSO

ENSO is the largest natural mode of interannual climate variability in the tropics; oscillations between warm and cold phases occur on a 2- to 7-year timescale, and the effects are felt worldwide (Timmermann et al., 2018). Here we present a selection of ENSO metrics giving an overview of model performance (Table 3). These

Table 3

Selection of ENSO Performance Measures for N216ORCA025 (300 years), N96ORCA1 (500 years) and Observations

Metric	Observations	N216ORCA025	N96ORCA1
M1 σ_{SST} at N3 ^a	0.79	0.76 (0.69–0.79)	0.79 (0.69–0.86)
M2 σ_{SST} at N4 ^b	0.54	0.48 (0.43–0.51)	0.61 (0.50–0.67)
M3 Timescale of SST at N3	72.1	55.4 (48.5–68.2)	51.8 (32.0–67.0)
M4 Ratio of σ_{SST}^{winter} to σ_{SST}^{spring}	1.6	1.3 (1.2–1.4)	1.3 (1.1–1.5)
M5 σ_{precip} at N4	2.3 ^c ; 2.7 ^d	2.3 (2.2–2.4)	1.9 (1.6–2.1)
M6 SST at N3	25.7	25.9 (25.8–26.0)	25.4 (25.3–25.5)
M7 τ_x at N4 ($\times -1,000$)	34	34 (35–37)	42 (41–44)

Note. Values in brackets show the range determined from a 100-year moving window in the respective model. Metric 1 (M1) and metric 2 (M2) are the standard deviation of the monthly SST anomaly (Kelvin) for regions Niño3 (90–150°W, 5°N–5°S) and Niño4 (160°E to 150°W, 5°N to 5°S). M3 is the ratio of power (in percent) in the 3- to 7-year range relative to 0–10 years for monthly Niño3 SST anomalies. M4 is a seasonality metric defined as the ratio of November to January and March to May standard deviation of Niño3 SST anomaly. M5 is the standard deviation of precipitation anomalies for Niño4 (millimeter per day). M6 is the annual mean SST for Niño3 (K), and M7 is the annual mean zonal wind stress for Niño4 ($-1,000 \text{ Nm}^{-2}$). SST observations are HadISST (1911–2010; Rayner et al., 2003), precipitation is GPCP v2.2 (1979–2013; Adler et al., 2003) and CMAP (in brackets, 1979–2015; Xie & Arkin, 1997), and wind stress is the SOC climatology (Josey et al., 1998); CMAP = Climate Prediction Centre Merged Analysis of Precipitation; HadISST = Hadley Centre Sea Ice and Sea Surface Temperature.

^aN3: Niño3 region. ^bN4: Niño4 region. ^cUsing GPCP. ^dUsing CMAP. ENSO = El Niño–Southern Oscillation; SST = sea surface temperature.

can be compared to Williams et al. (2018) and Kuhlbrodt et al. (2018) for recent HadGEM3 configurations and Bellenger et al. (2014) for CMIP3 and CMIP5 models.

The amplitude of SST variability in the east Pacific (Metric 1, M1) is similar in both N216ORCA025 and N96ORCA1, with standard deviations (of monthly anomalies) of 0.76 and 0.79, respectively. This compares with the observed value of 0.79 for HadISST1.1. Both models exhibit low-frequency variability, such that if a 100-year moving window is applied to N96ORCA1, the standard deviation varies from 0.69 to 0.86. As such, observations lie within the model range. There may be a small upward trend in variability in the models, suggesting a slow drift, but longer experiments would be needed to confirm this. In the central Pacific variability is higher in N96ORCA1 than in N216ORCA025 and observations (M2). It can be seen from the El Niño spatial pattern that variability extends too far west in N96ORCA1, with the zero line occurring about 15° to the west in N96ORCA1 compared to N216ORCA025 (Figure 1). This westward extension of the ENSO pattern is a common feature in many lower-resolution climate models (Guilyardi, 2006; Roberts et al., 2018; Shaffrey et al., 2009; Van Oldenborgh et al., 2005). Comparison with earlier versions of HadGEM3 at different resolutions suggests that both the ocean and atmosphere resolution play a role, although the ocean appears to be the more important. SST variability is also less well simulated in N96ORCA1 in the far east Pacific, where variability is too low. Neither model is able to correctly reproduce the observed ENSO asymmetry in the east Pacific, with both showing skewness for region Niño3 close to zero.

A power spectrum analysis of east Pacific SST shows that, in agreement with observations, variability lies within the 2- to 7-year timescale for both N96ORCA1 and N216ORCA025 (Figure 2 and M3). Similar to the present-day control, there is perhaps a little more power in the 2- to 3-year timescale than observed (Kuhlbrodt et al., 2018). ENSO variability is closely phase locked to the annual cycle with variability at a maximum in early boreal winter and a minimum in spring. Both models capture this seasonality (M4) although N96ORCA1 extends the maximum variability through to late winter/early spring.

The variance of precipitation in the west Pacific (M5), which gives an indication of the impact of tropical Pacific variability on the large-scale circulation, is slightly greater in N216ORCA025 than in N96ORCA1 and agrees well

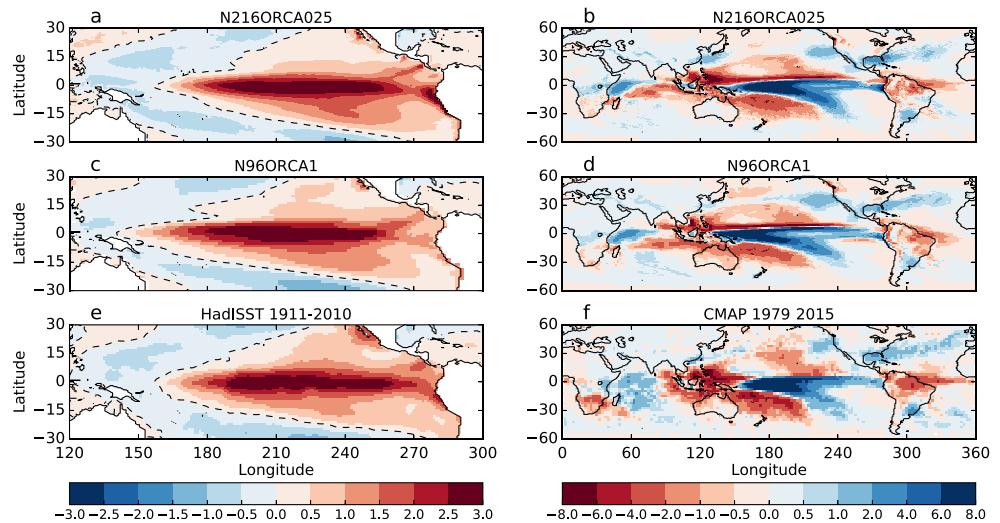


Figure 1. El Niño December–February composites of events with a Niño 3.4 sea surface temperature anomaly greater than 0.8 K for sea surface temperature (K) and precipitation (mm/day) for N216ORCA025 (a, b), N96ORCA1 (c, d), the HadISST1.1 data set (period 1911–2010, e), and the CMAP precipitation data set (1979–2015, f). Dashed lines mark zero contour in panels a, c, and e. CMAP = Climate Prediction Centre Merged Analysis of Precipitation; HadISST = Hadley Centre Sea Ice and Sea Surface Temperature.

with observations. The area of maximum precipitation in the west Pacific associated with El Niño is shifted to the west in N96ORCA1 (Figure 1d) compared to N216ORCA025 (Figure 1b), and the impact of the equatorial cold bias (see below) is evident to the east of the dateline where the lower-resolution model appears less well able to support convection. The main precipitation teleconnections are reproduced by both models but are weaker than observed (Figure 1f). They also appear weaker than the present-day control experiments (not shown).

Accurate representation of the mean zonal structure of the equatorial Pacific has proved challenging for both CMIP3 and CMIP5 models (their Figure 6; Bellenger et al., 2014). Overall, N216ORCA025 reproduces the magnitude of the SST and SST gradient well, while, in common with many climate models; N96ORCA1 shows an equatorial cold bias (Figure 3a). Enhanced equatorial heat transport due to tropical instability waves likely plays a key role and has been shown to be well represented by the ORCA025 ocean (Graham, 2014). Both models are too warm in the upwelling/stratocumulus region in the far eastern Pacific, with the larger bias in N96ORCA1. Ocean resolution appears to play a dominant role in these areas (Hewitt et al., 2016). Note that for N96ORCA1 the cold and warm biases tend to cancel for the Niño3 region (M6). The equatorial zonal mean wind stress in N216ORCA025 agrees well with observations except to the west of the dateline where there are

overly strong easterlies. In association with the model cold bias, N96ORCA1 has an easterly bias over much of the central and west Pacific (Figure 3b, M7).

2.2. NAO

The NAO is a key mode of winter variability for the North Atlantic and surrounding continents on seasonal to multidecadal timescales (e.g., Hurrell, 1995). In this analysis, the winter NAO index is defined as the leading principal component of December to February mean sea level pressure (MSLP) in the North Atlantic (90°W to 40°E, 20–90°N), with similar results (not shown) found using the difference in MSLP anomalies for the closest grid points to the Azores (37.7°N, 25.7°W) and Iceland (65°N, 22.8°W; Jones et al., 1997). For comparison against real-world MSLP the twentieth Century Reanalysis is used (Compo et al., 2011) for the period 1871–2011, which has good observational coverage and MSLP variability very similar to that of the model (standard deviation of point based anomaly NAO index is 8 hPa in both the models and observations).

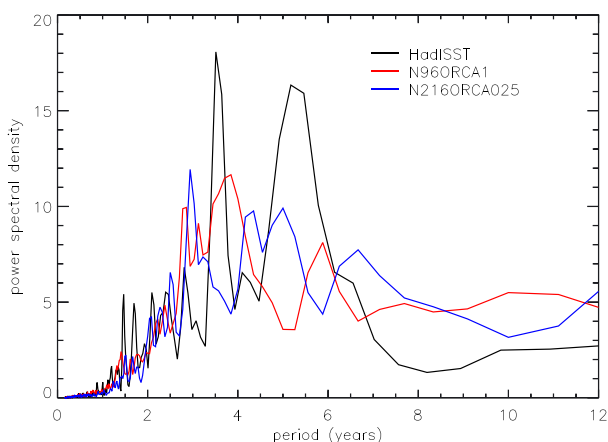


Figure 2. Niño3 (90–150°W, 5°S to 5°N) sea surface temperature anomaly power spectra (K^2) for N216ORCA025 (blue, 300 years), N96ORCA1 (red, 500 years), and the HadISST observational data set (black 1911–2010).

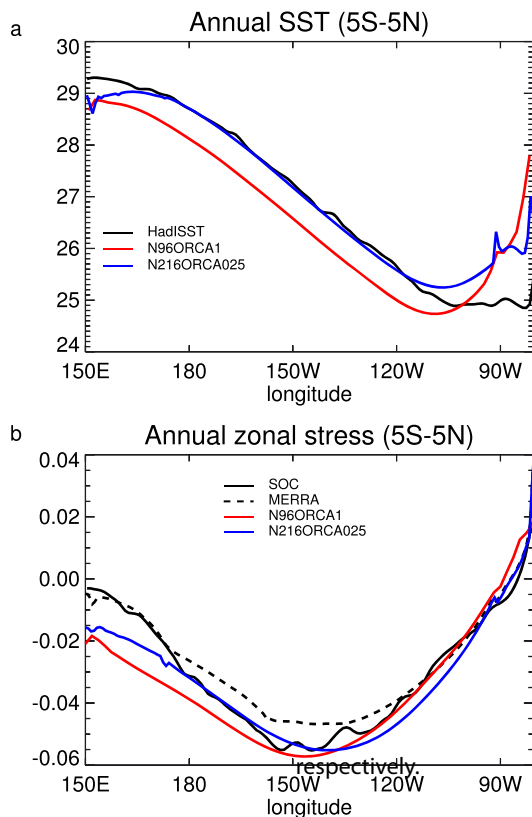


Figure 3. Annual mean Pacific SST (a) averaged over 5°N to 5°S for N216ORCA025 (blue), N96ORCA1 (red), and HadISST1.1 (period 1911–2010, black). Annual mean Pacific wind stress (b) averaged over the same region for N216ORCA025 (blue), N96ORCA1 (red), and MERRA (1982–2001, black, dashed; Rienecker et al., 2011) and Southampton Oceanography Centre climatology (1980–1993, black, solid; Josey et al., 1998) observations. SST = sea surface temperature.

The N216ORCA025 and N96ORCA1 winter seasonal mean NAO distributions are almost identical (also close to observations, not shown). However, N216ORCA025 shows signs of greater variability on multidecadal timescales than N96ORCA1 (Figure 4). The aggregated mean variance (Figure 4a) is the variance of multiyear mean values calculated from a time series for increasing rolling window periods. It is used as a measure of how quickly values in a time series become independent of one another, with truly independent values leading to variance inversely proportional to the period length (cf. diagonal line in Figure 4a). The observed NAO exhibits long-range dependence, with aggregated mean variance above the diagonal, up to about 50-year periods as found in other studies (e.g., Stephenson et al., 2000). N216ORCA025 exhibits comparable variances to observations out to 10 years and long-range dependence out to 30 years. In contrast, N96ORCA1 has variances on or below the diagonal throughout, suggesting a lack of long-range dependence. A similar method is used to assess the variability of the linear trend of the NAO on different timescales, with N216ORCA025 generally having higher variability than N96ORCA1 and again being closer to the observations, though with higher variability for shorter periods (Figure 4b). N216ORCA025 exhibits higher NAO trends than seen in N96ORCA1 for the standardized empirical orthogonal function-based index and also for alternative absolute indices such as a station-like definition for which 30-year maximum trends are 0.56, 0.58, and 0.37 hPa/year for observations, N216ORCA025 and N96ORCA1,

The spectral analysis of NAO variability (Figure 4c) shows that N216ORCA025 has higher multidecadal variability than N96ORCA1 and maintains this for longer periods as seen in the observations. Recent studies have found that GCMs generally underestimate the observed NAO low-frequency variability, including a comprehensive analysis of CMIP5 models (Bracegirdle et al., 2018a; Kim et al., 2018; Kravtsov, 2017); thus, it is of interest that increased resolution may help models to better simulate multidecadal NAO trends. This could be related to the improvements seen in seasonal variability of Atlantic winter blocking, attributed to reduced SST biases in the North Atlantic in high-resolution models (Scaife et al.,

2011). In addition, a 30-year mean smoothing of the NAO time series suggests that N216ORCA025 and observations have stronger negative NAO periods than N96ORCA1 (Figure 4d), so perhaps the latter is lacking the mechanisms needed to produce such strong negative events though neither model resolution properly captures the observed distribution.

Despite this difference in decadal variability, the associated multiyear atmospheric teleconnection patterns are very similar for the two model resolutions, for example, for 30-year mean NAO regression patterns with geopotential height at 500 hPa, MSLP, surface air temperature, and precipitation (not shown). This is consistent with recent work that found that CMIP5 models all have a fairly reasonable representation of the NAO pattern in terms of spatial correlation, despite showing variations on how well the models simulate the associated physical processes (Davini & Cagnazzo, 2014).

2.3. Tropical Intraseasonal Variability

Tropical intraseasonal variability is dominated by the MJO (Madden & Julian, 1971), which is characterized by an eastward propagation of deep convection and associated wind structures moving along the equator with an average phase speed of around 5 m/s with periods between 30 and 90 days. The eastward propagation is more pronounced during Northern Hemisphere (NH) winter months, while there is a dominant northeastward movement during Boreal summer months associated with the Asian summer monsoon (Zhang, 2005). Tropical variability is also influenced by the equatorial waves, namely, the equatorial Rossby waves, Kelvin waves, mixed Rossby-gravity waves, and the inertia-gravity waves (Wheeler & Kiladis, 1999).

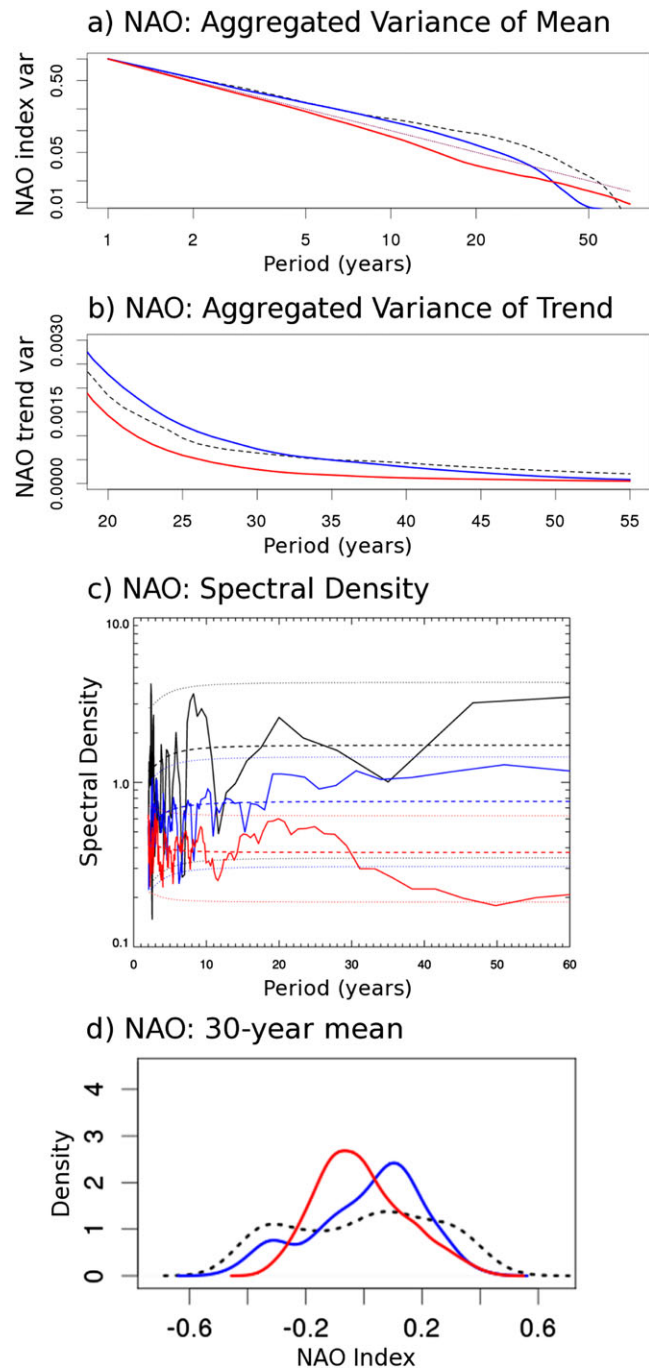


Figure 4. The variance of the multiyear mean of the wintertime NAO index (a) and linear trend (b) for increasing rolling window periods, the spectral density of the NAO versus the period of variability (c), and the probability density function of 30-year means of the wintertime mean NAO index (d) for N216ORCA025 (blue), N96ORCA1 (red), and reanalysis (black dashed line: a, b, d; black solid line: c; period 1871–2011). The dotted diagonal line in (a) represents the 1–1 log ratio; points above this suggest long-range dependence, while points below this suggest long-term switching behavior. As a measure of significance, dashed lines in (c) represent the spectrum of the associated red noise processes with their 95% confidence spectrum shown by the dotted lines. NAO = North Atlantic Oscillation.

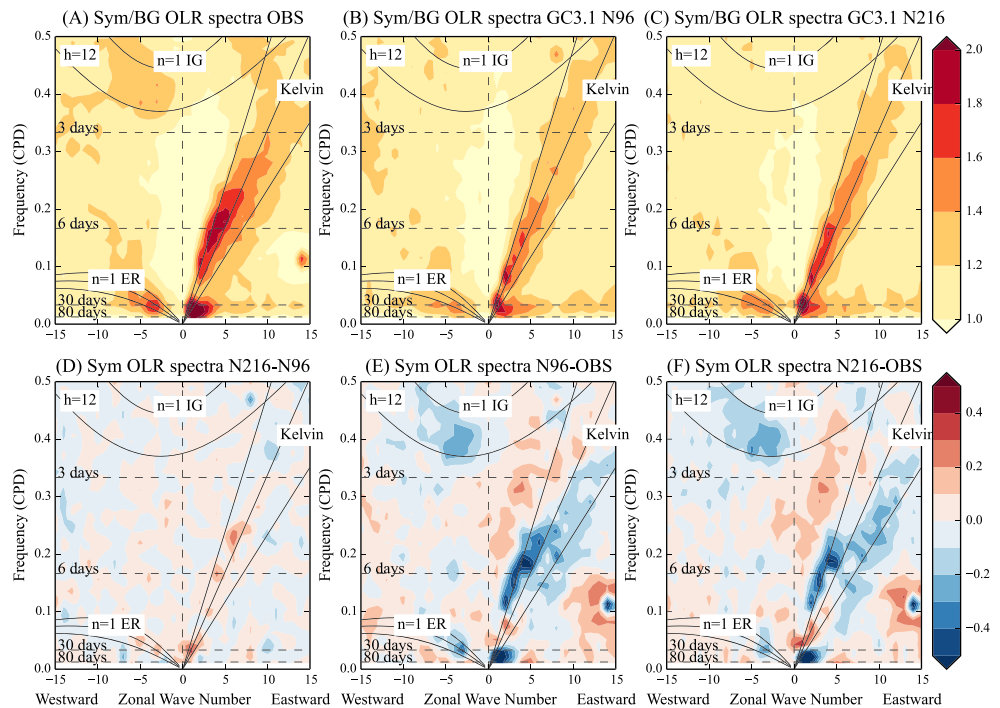


Figure 5. The ratio between raw power spectrum of outgoing longwave radiation (OLR) and a background spectrum (top row) from observations (1979–2013, a), N96ORCA1 (b), and N216ORCA025 (c). The differences in raw power spectrum (bottom row) between the HadGEM3-GC3.1 model resolutions (d) and the differences between these two model resolutions and observations (e, f). All values are log of OLR power. See Wheeler and Kiladis (1999) for details. CPD = Cycles per day.

This section evaluates the tropical wavenumber-frequency spectra (Wheeler & Kiladis, 1999) in the two model resolutions in comparison with the observed spectra (based on satellite observations). Figure 5 (top row) shows the symmetric wave spectra expressed as the ratio of raw power of outgoing longwave radiation (OLR) and a smoothed background spectra that highlights the major equatorial wave modes and their dispersion relationships compared to that of a shallow water model (represented as lines). Here OLR is used as a proxy for cloud top height, which is influenced by the strength of convective activity. Both N96ORCA1 and N216ORCA025 produce much weaker variability at all scales than the observations, particularly for Kelvin and MJO modes (wavenumbers 1–3 and periods 30–90 days). The bottom row shows the difference plots which highlight the lack of wave power at the dominant equatorial wave modes and MJO. The difference between N216ORCA025 and N96ORCA1 (Figure 5d) suggests that there is an increased Kelvin wave power and not much difference for any other wave properties. Both model versions produce a consistent lack of inertia-gravity waves.

The MJO is known to be a difficult phenomenon to represent in global models (Jiang et al., 2015). The Unified Model is known to produce a relatively weak MJO propagation in most model intercomparison studies (Kim et al., 2014). Much effort was put in to understand this model behavior, particularly the role of convective entrainment (Klingaman & Woolnough, 2014; Walters, Boutle, et al., 2017) and air-sea interactions (DeMott et al., 2016) in the Unified Model. A description of the model components and the impact of various physics changes in the development of HadGEM3-GC3.1 are provided in Williams et al. (2018). Due to the differences in the main features of Tropical Intraseasonal Variability with season, the propagation characteristics are examined separately for boreal winter and summer. Figure 6 (left column) shows the MJO propagation as lead-lag correlation values of intraseasonal convection (OLR) and 850-hPa wind anomalies with respect to a reference time series. The meridionally averaged correlation values of convection anomalies in the boreal winter season—with respect to a time series over equatorial Indian Ocean (70–100°E, 10°S to 10°N)—highlight the eastward propagation of OLR anomalies from the Indian Ocean to the west Pacific. It is coincident with the regions of 850-hPa zonal wind convergence (Figure 6a). In both model versions, the OLR anomalies are weaker with subdued propagation characteristics. The correlation values of 850-hPa wind anomalies with respect to

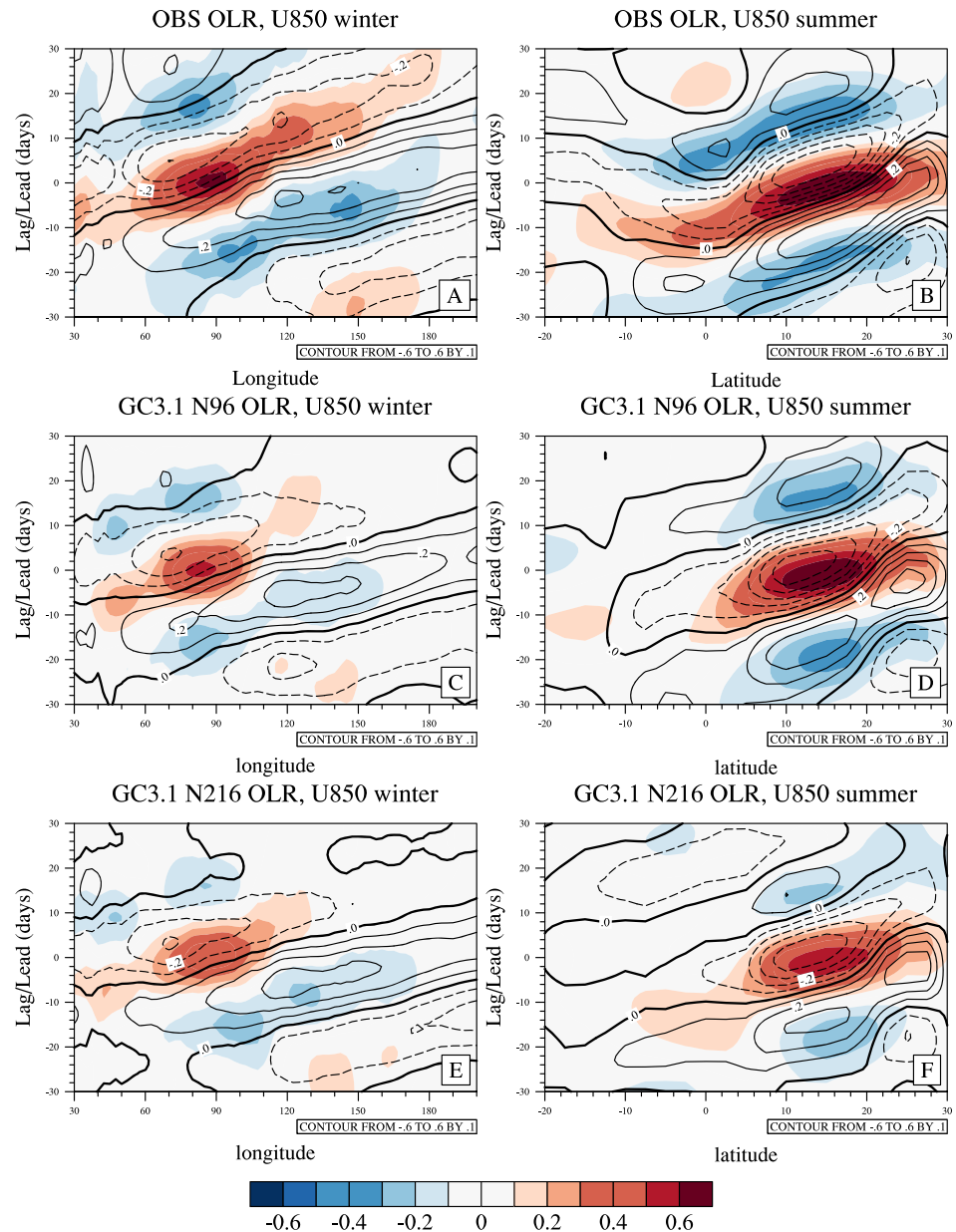


Figure 6. Hovmöller plot of OLR correlation coefficient (color shades) at all grid points with a reference time series defined as OLR averaged over 70–100°E, 10°S to 10° N as a function of lead/lag. The similar correlation of U850 with the OLR reference series is plotted as contours. Positive values are represented by solid contours and negative values by dashed contours. The same contour levels are used for both OLR and U850. Time progresses upward. OLR = outgoing longwave radiation.

OLR are weaker in the model even though the wind propagation is much better than that of OLR. Generally, the models produce weaker but faster eastward propagation compared to the observations.

The northward propagating monsoon intraseasonal oscillations (MISO) are shown in a similar manner except that the correlation values are zonally averaged for the Bay of Bengal region (70–100°E, 10–30° N) with respect to an averaged time series over the north Bay of Bengal (Figure 6, right column). The picture is similar to that of the eastward propagating MJO, with strong and coherent northward propagations in the observations. The convection signals in N96ORCA1 appear to be slightly stronger than in N216ORCA025. Both models generate reasonable northward propagation both in OLR and winds. In summary, GC3.1 has improved intraseasonal variability compared to the previous model version (Williams et al., 2018) and it appears that the

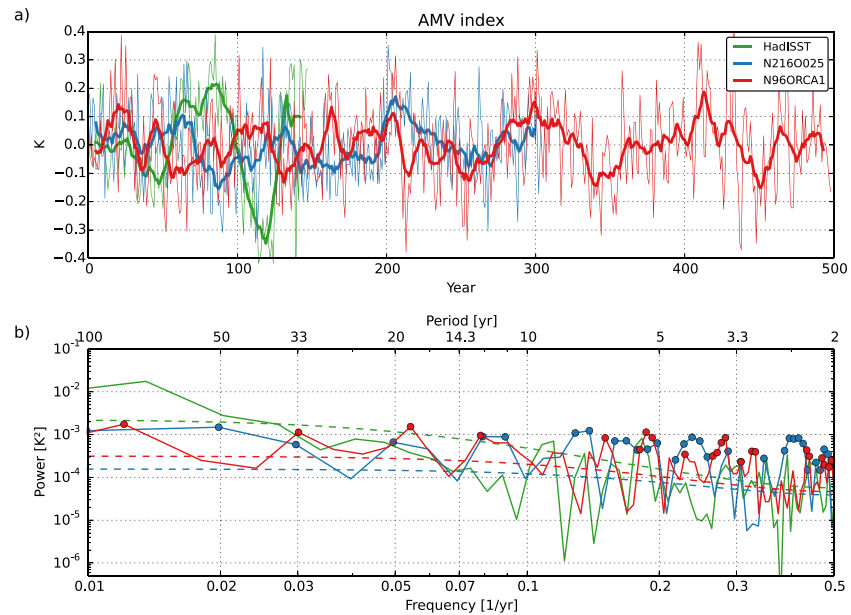


Figure 7. Linearly detrended AMV index (a) for N216ORCA025 (blue), N96ORCA1 (red), and the HadISST observational data set (green; Rayner et al., 2003). The year count is for the model simulations; the HadISST data actually cover 1870 to 2017. Thin lines show annual means and thick lines an 11-year moving average. Power spectrum (b) of the annual mean time series using a Bartlett window. A theoretical AR(1) spectrum, based on the estimated autocorrelation coefficient, is given as a dashed line for each spectrum. The dots mark those frequencies where the spectral power is above the 95% confidence interval around the AR(1) spectrum. AMV = Atlantic Multidecadal Variability; HadISST = Hadley Centre Sea Ice and Sea Surface Temperature.

increased horizontal resolution of the model has only minor impacts on the amplitude of equatorial Kelvin waves and little impact on the character of MJO/MISO propagation.

2.4. AMV

Multidecadal variability in the Atlantic (AMV) has been linked with decadal variability in rainfall in the Sahel region (Zhang & Delworth, 2006), precipitation over Europe (Sutton & Hodson, 2005), and hurricanes in the tropical Atlantic (Goldenberg et al., 2001). Defined as the basin-scale average of sea surface (or surface air) temperatures, minus a reference mean (often the global mean), it is a climate index that appears to have long period variability in paleorecords (Gray et al., 2004), instrumental observations (Schlesinger & Ramankutty, 1994), and climate models (Knight et al., 2006).

The AMV time series were calculated as the difference between the annual SST anomalies for the North Atlantic (0–60°N) and the global SST anomalies (after Trenberth & Shea, 2006), for the simulations and the observations. The two simulated time series in Figure 7a look similar at first sight. However, their lag = 1 autocorrelation coefficients (α) are different, with $\alpha_{N216} = 0.33$ for N216ORCA025 and $\alpha_{N96} = 0.44$ for N96ORCA1. The 95% confidence interval for α_{N96} is [0.37, 0.51], and hence, α_{N96} lies outside of the range of α_{N216} . In other words, in the higher-resolution model version (N216ORCA025) there is more variance on the shorter timescales, and less on the longer timescales, than in the lower-resolution version. The time series from HadISST (green) displays an autocorrelation (α) of $\alpha_{Had} = 0.73$, much larger (and significantly so, with 95% confidence intervals of [0.64, 0.79]) than in the simulations. This reflects the strong 70-year oscillation in the twentieth century observational data. In the simulations, such oscillations also occur (e.g., in N96ORCA1 between years 250 and 400), though with a reduced amplitude and more sporadically.

The power spectra (Figure 7b) depict the discussed variability properties in a different way. In HadISST, most of the variance occurs around periods of 70 years. Conversely, the model simulations have more variance on the interannual timescales (period of 5 years and less). For some decadal period bands the attributed variance is significantly different from red noise. Examples are 80, 33, 18, and 12.5 years in N96ORCA1 and 50–100, 17, and 13 years in N216ORCA025. Some of these timescales may be related to self-sustaining periodic variability in the NA SPG, for which the mechanisms (and thus timescales) are different across the resolutions.

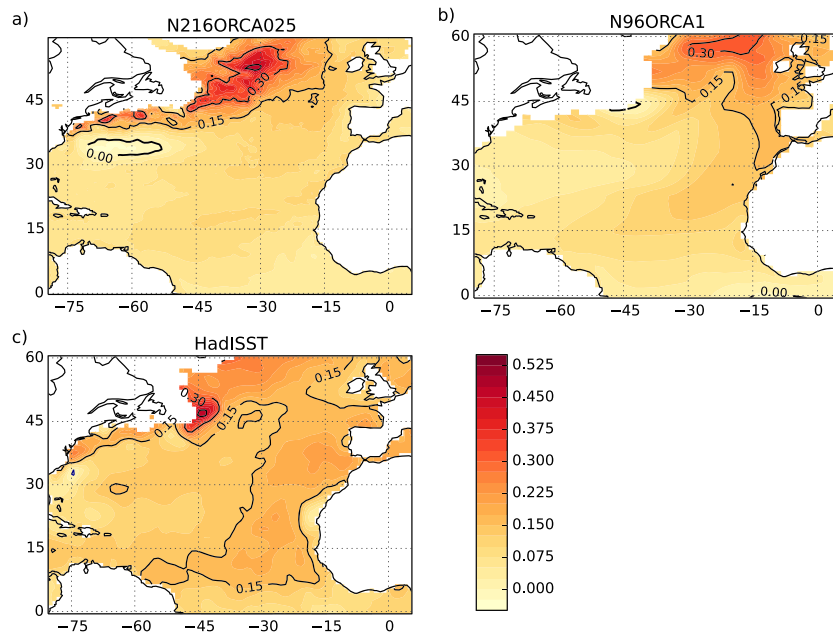


Figure 8. Sea surface temperature regressed against the Atlantic Multidecadal Variability index, both low-pass filtered (cutoff period 10 years), for N216ORCA025 (a), N96ORCA1 (b), and the HadISST data (c). Areas that are (sometimes) sea ice covered have been masked. The interval for the solid black contours is 0.15.

The width of the analytic 95% confidence interval depends, among other parameters, on the length of the time series and so for the comparatively short HadISST time series no periods emerge as significantly different from red noise. Overall, the two simulated time series have a fairly similar distribution of their variance across the periods, while the observations have more variance on the long timescales. The similarity between the two resolutions is in contrast to the NAO power spectra, where more low-frequency (multidecadal) variability is found in N216ORCA025 (Figure 4); perhaps this is masked in the AMV index by tropical variability (or lack thereof; see next). In addition, while the preindustrial simulations we analyze here contain no forced variability by construction, it is likely that some fraction of the variability in HadISST is caused by anthropogenic forcing (Booth et al., 2012). This limits the direct comparability between the simulated and observed time series.

The spatial pattern of the AMV, diagnosed as the regression of the SST anomalies against the AMV index (Figure 8), is marked by a small region just off the Grand Banks that correlates very strongly with the AMV index (Figure 8c) and by this correlation otherwise being larger in the eastern and northern parts of the North Atlantic. Neither model version fully renders this pattern. In N216ORCA025 (Figure 8a), the Grand Banks correlation maximum stretches over large parts of the subpolar northwest Atlantic. In N96ORCA1 (Figure 8b), there is actually almost no correlation of the SST with the AMV index in the Grand Banks region, and the maximum is found south of Iceland instead. This northeastward shift may be related to there being far less deep water formation in the Labrador Sea region in N96ORCA1 than in N216ORCA025 (not shown; but see discussion in section 2.7). Nonetheless, in both Figures 7 and 8, the comparison is between unforced variability in the simulations and partially forced variability in the observations. Hence, the shifted foci of the patterns in Figure 8 could also be a sign of the model's insufficient internal variability, or of the forced variability imprinted on the observations, or a mixture of both.

2.5. Stratospheric Variability and the QBO

Variability in the stratosphere is dominated at polar latitudes by vortex variability in winter, especially in the NH, and at equatorial latitudes by the QBO. The ability of models to reproduce the strength and variability of both the polar vortex and the QBO is important if teleconnections are to be investigated.

An indicator of NH polar vortex variability is the time series of zonally averaged zonal winds at 60°N, 10 hPa (Figure 9). As the season moves from summer to autumn/early winter the climatological zonal winds reverse from weak easterly to strong westerly flow, driven by seasonal variations in radiative forcing that determine the latitudinal temperature gradients. This westerly polar vortex can reach speeds in excess of 80 m/s. However, the vortex strength is intermittently damped by the action of planetary-scale Rossby waves that propagate vertically from the troposphere into the stratosphere and then break when their amplitudes

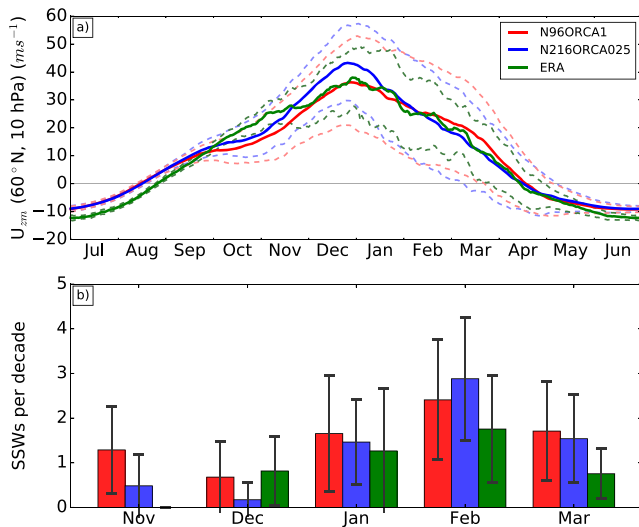


Figure 9. Time series (a) of daily averaged zonally averaged winds (m/s) at 60°N and 10 hPa. Solid lines indicate the mean wind, and dashed lines indicate the 1 standard deviation range for simulations and the ERA-40 (1958–1978; Uppala et al., 2005) plus ERA-Interim (1979–2018; Dee et al., 2011) reanalyses. Bar chart (b) of number of SSWs per decade from the N96ORCA1 (red) and N216ORCA025 (blue) simulations compared with the reanalyses for the period 1958–2018 (green). Whiskers indicate the 1 standard deviation range. SSW = sudden stratospheric warming.

become too large to be sustained, thereby transferring their easterly momentum to the background flow (Andrews et al., 1987). If the wave forcing is sufficiently large and/or prolonged, and depending on the background flow which influences the precise direction of wave propagation, this wave forcing can break down the vortex so that the zonal winds temporarily reverse to become easterly. This is known as a sudden stratospheric warming (SSW) since the associated polar temperatures increase dramatically in just a few days (e.g., Butler et al., 2015; McInturff, 1978).

SSWs are the prime source of interannual variability in the NH stratosphere, and their influence can extend deep into the troposphere to influence surface weather patterns, including the NAO (Baldwin et al., 2001; Thompson & Wallace, 1998). A good representation of polar vortex variability is therefore of importance for investigating stratosphere-troposphere teleconnections, especially in winter. Figure 9a indicates that the model at both N96ORCA1 and N216ORCA025 resolutions captures the observed variability well, perhaps not surprising because of the large-scale nature of the relevant waves. The ensemble mean of the simulations lies within the observed 1 standard deviation range throughout the winter (December–February inclusive) period, and the timing of the final warming in mid-April is captured particularly well. In summer and in autumn/early winter, on the other hand, there are evident biases. At both resolutions the summer easterlies are consistently too weak (July–August) and in early winter (October–November) the polar vortex westerlies are too weak; the latter is especially evident in N96ORCA1 where the ensemble mean falls below the 1 standard deviation envelope of the observations.

The weak polar vortex in November is also apparent in Figure 9b that shows the number of SSWs per decade in each model version, as a function of month, compared with reanalysis data. The SSW identification employs the methodology of Charlton and Polvani (2007), and only midwinter SSWs are included. If only the December to March months are considered, then both model resolutions do reasonably well in terms of the average frequency of SSWs over the extended middle to late winter. There is some indication that the modeled SSWs occur slightly later than observed, for example, with too few in December and too many in March, possibly a sign of the *cold-pole* problem (Hamilton et al., 1999). On the other hand, the model exhibits unrealistically early SSWs in November and thus suffers from being too warm and disturbed in early winter. Given that the vortex takes a few weeks to recover from an SSW, this could explain the relative sparsity of SSWs in December. The increased resolution in N216ORCA025 improves upon the warm bias in November, perhaps due to improved resolution of the tropospheric processes that generate the Rossby waves or due to improved representation of the background wind gradients in the stratosphere that influence their propagation. However, the improved resolution does not improve the cold bias in December, suggesting that there may be other influencing factors as well.

Interannual- and decadal-scale variability of the polar vortex is influenced by a number of different factors, including the QBO (Baldwin et al., 2001), ENSO (Barriopedro & Calvo, 2014), major volcanic eruptions (Robock, 2000), and variations in solar irradiance (Gray et al., 2010). Here we further examine the model representation of the QBO and its impact on the polar vortex.

The QBO is the leading mode of zonal wind variability in the equatorial stratosphere. It is observed as alternating easterly and westerly phases descending from around 1 to 70 hPa with a phase period of approximately 28 months at 30 hPa (for a review, see Baldwin et al., 2001). HadGEM3-GC3.1 employs a parameterized non-orographic gravity wave scheme (Scaife et al., 2002) that supplements the vertical waves resolved by the model, resulting in a realistic and spontaneously generated QBO. By comparing the observations, using the Freie Universität Berlin (Kunze, 2017) zonal wind data set, with the equatorial stratospheric zonal mean zonal winds of the N96ORCA1 and N216ORCA025 simulations (Figure 10), we find that the simulated equatorial winds have similar structure and downward phase propagation to observations.

We calculate the QBO index for the model as the area-averaged zonal winds between 5°N and 5°S for the particular level of interest. The observed QBO index uses the Freie Universität Berlin data set. A threshold of

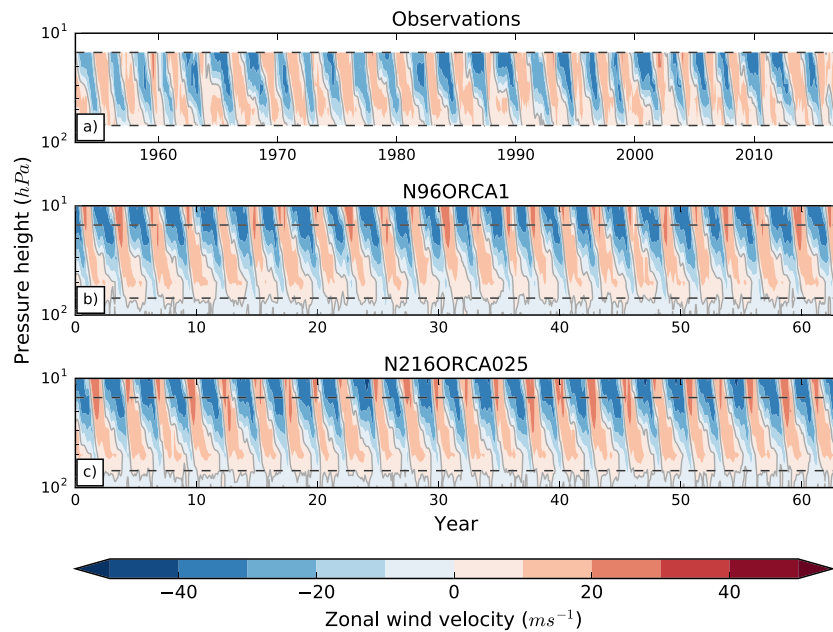


Figure 10. Hovmöller diagram showing the zonal wind evolution of the Freie Universität Berlin observational data set 1953–2016 (a) and the area-averaged equatorial zonal mean zonal wind evolution between 5°S and 5°N over a 63-year period of N96ORCA1 (b) and N216ORCA025 (c) preindustrial control simulations. The dashed horizontal lines at 15 and 70 hPa are for guidance only.

± 5 m/s is applied to the QBO index when making composites of geopotential height (GPH) for QBO westerly (QBO-W) minus QBO easterly (QBO-E) conditions to remove neutral cases. A comparison of the maximum, minimum, and standard deviation of the QBO indices at various levels (Table 4) shows that the simulations are similar to observations at 15 and 30 hPa but are slightly weaker at 50 hPa. Analysis of QBO-E to QBO-W transitions at 30 hPa indicates that the simulated QBO mean period is 3–4 months longer than observed (observations: 27.9 months; N216ORCA025: 30.7 months; N96ORCA1: 31.8 months), with standard deviations smaller by approximately 1 month (observations: 3.6 months; N216ORCA025: 2.5 months; and N96ORCA1: 2.9 months). Nonetheless, the level of agreement provides confidence that the HadGEM3-GC3.1 preindustrial control simulations are generally able to reproduce a QBO similar to that observed in the present era.

Observational and model studies suggest the existence of teleconnections between the QBO and the NH winter surface climate. One possible route of QBO influence is via its modulation of the NH polar vortex, which then influences the surface as described earlier. Composite QBO-W minus QBO-E differences in reanalyses show a strengthened NH polar vortex and a positive Arctic Oscillation structure that extends to the surface that is particularly evident in the NAO region (Anstey & Shepherd, 2014; Holton & Tan, 1980). Additional QBO influence routes are an ongoing topic of interest (see, e.g., Figure 1 of Gray et al., 2018, and references therein) such as via the subtropical jet (Garfinkel & Hartmann, 2011; Ruti et al., 2006; Simpson et al., 2009) and the direct impact of the QBO on tropical deep convection (Gray et al., 2018; Liess & Geller, 2012).

Table 4
Comparison of the Strength and Standard Deviation of the Monthly QBO Winds at Different Heights in Observations and HadGEM3-GC3.1

QBO level (hPa)	Strength (m/s)								
	Observations			N96ORCA1			N216ORCA025		
	Max	Min	S.D.	Max	Min	S.D.	Max	Min	S.D.
15	28	−40	20	22	−35	18	19	−28	13
30	26	−39	22	20	−31	16	16	−20	8
15	26	−40	23	21	−30	16	16	−19	8

Note. QBO = Quasi-Biennial Oscillation.

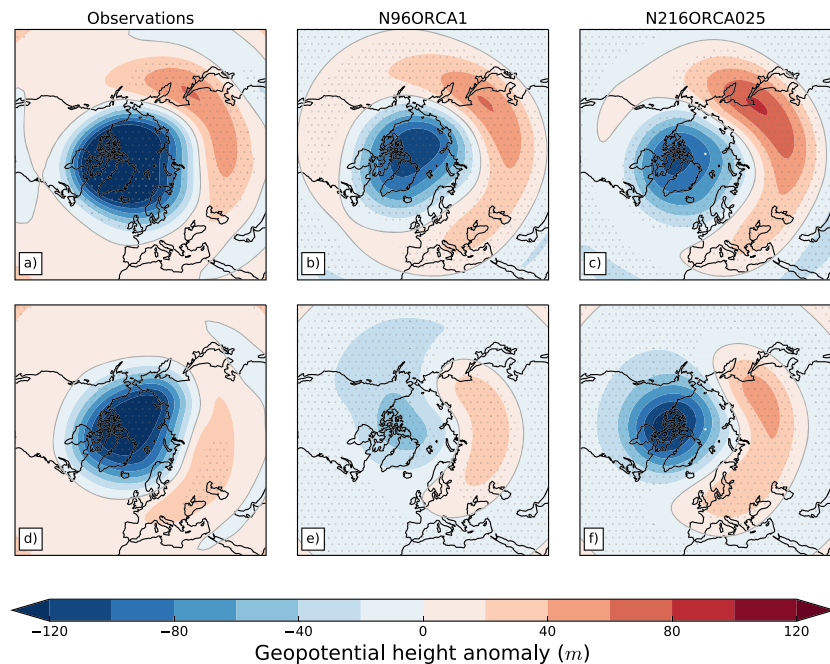


Figure 11. Winter (December-January-February) response of the detrended geopotential height at 50 hPa to the detrended QBO at two different levels for observations (a, d), N96ORCA1 (b, e), and N216ORCA025 (c, f). The first row (a–c) is the response to the Quasi-Biennial Oscillation at 50 hPa and the second row (d–f) to 30 hPa. Stippled regions are significant above the 95% level. The observed response is calculated using the geopotential height data set from the National Centers for Environmental Prediction/National Center for Atmospheric Research Reanalysis (Kalnay et al., 1996).

To explore the stratospheric polar vortex route, we show QBO-W minus QBO-E composite differences of the linearly detrended GPH fields at 50 hPa (GPH50; Figure 11). Detrended QBO indices at 30 and 50 hPa are used to characterize the QBO winds, in order to explore the response to different QBO heights. The rationale for this approach is that the teleconnection mechanisms and the optimal QBO index height are ongoing topics of research. The observed GPH50 polar response to the QBO index at 50 hPa (Figure 11a) shows a negative polar region with a positive band in the midlatitudes centered over East Asia. The preindustrial control runs show similar positive patterns to observations in the midlatitudes (Figures 11b and 11c), with a weaker but significant negative polar region. This is evidence of the *Holton-Tan effect* which links the QBO to the stratospheric polar vortex (Holton & Tan, 1980). Analysis of the GPH50 response to the QBO index at 30 hPa (Figures 11d–11f) is similar to the response to the index at 50 hPa but with weaker negative polar regions, especially for N96ORCA1. This suggests that the extratropical GPH50 response to the vertical structure of the equatorial QBO differs between resolutions.

2.6. ACC

The eastward flowing ACC, extending throughout the entire Southern Ocean around the globe, is the strongest current globally and connects all three major ocean basins. It is driven by the westerly winds and the surface buoyancy fluxes between 40°S and 60°S, both of which act to steepen the isopycnal layers in the meridional direction. This is balanced by mesoscale eddies acting to flatten the isopycnal layers and hence reduce the meridional density gradient in the upper layer of the Southern Ocean (Marshall & Radko, 2003). The ACC is geostrophically balanced by the isopycnal layers sloping upward toward Antarctica, which is reflected in the meridional gradient of sea surface height.

By convention, the ACC strength is defined as the volume transport through the Drake Passage. Elsewhere, in the absence of continents, the current's boundaries are generally defined by meridional variations in specific water properties of the Southern Ocean (Orsi et al., 1995). The mean baroclinic flow through the Drake Passage has been measured to be 137 ± 8 Sv (Cunningham et al., 2003). However, over complex bottom topography 20–50% of the total flow is barotropic and, when this is included, the estimate of total Drake Passage transport becomes 173.3 ± 10.7 Sv (Donohue et al., 2016).

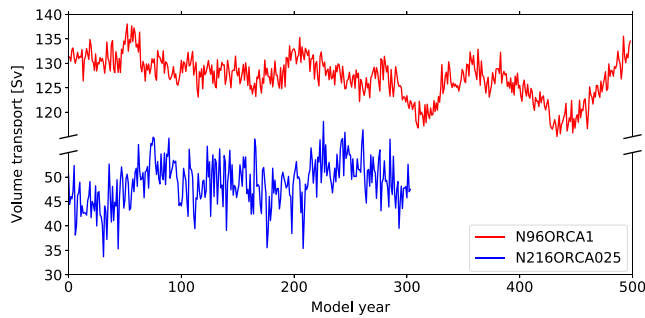


Figure 12. The annual mean total Antarctic Circumpolar Current transport through the Drake Passage in HadGEM3-GC3.1. Note the break in the y axis; interval spacing remains the same.

Here we describe the differences in mean state and variability of the ACC in N96ORCA1 and N216ORCA025. The first-order difference between the two models is the low transport in N216ORCA025 (54 Sv) compared with N96ORCA1 (136 Sv; Figure 12). Consequently, we investigate if this can be attributed to differences in the forcing. The mean ACC transport in climate models may be influenced by the isopycnal diffusivity. If this is kept fixed, then it is dependent on the mean Ekman transport at the latitude of the Drake Passage and the thermohaline circulation (Gent et al., 2001). Among models participating in the CMIP3, the ACC transport significantly correlated with the coefficient for the mesoscale eddy parameterization (Kuhlbrodt et al., 2012). In addition, the interannual variability on the mean has been attributed to zonal mean wind stress (Mazloff, 2012) and the strength of the Ross Sea and Weddell Sea Gyres (Behrens et al., 2016).

The Southern Hemisphere annual mean maximum zonal mean wind speeds at the two model resolutions are similar at 10.75 ± 0.01 m/s (one standard error) at a latitude of 51.7°S , somewhat stronger than present-day observations from ERA-Interim of around 8.3 m/s at 53.1°S . In HadGEM3-GC3.1, the zonal mean time-averaged potential density (referenced to 2,000 m), a function of temperature and salinity, shows differences at the two-model resolutions (Figure 13). In the deep and midlatitude ocean the density and associated gradients are similar, with isopycnals outcropping to the surface at the latitude of the ACC. However, southward of 60°S the isopycnals in N216ORCA025 flatten at a greater depth than in N96ORCA1. This difference is associated with a large and permanent area of deep convection in the Weddell Sea in N216ORCA025. This artifact is common in CMIP5 models (Heuzé et al., 2013) and leads to significant heat uptake at depth. N96ORCA1 does not display such deep convection, possibly due to a lower Southern Ocean warm SST bias of 1 K, compared to 2.5 K in N216ORCA025 (Williams et al., 2018). The N216ORCA025 permanent region of deep convection, combined with the warm bias, leads to a reduced winter sea ice extent. The winter maximum sea ice extent (September mean) is 10.5×10^6 km² in N216ORCA025 and 15.5×10^6 km² in N96ORCA1, compared with present-day observations from HadISST of 18.1×10^6 km². Between the two model resolutions, a lower sea ice cover is not influencing the zonal mean winds as suggested by Bracegirdle et al. (2018b). In N96ORCA1, the shelf sea salinity is higher, which may be related to the lower simulated temperatures in this region leading to less local sea ice melt and the associated fresh water transported further north (see Williams et al., 2018, for discussion of the relevant processes).

The isopycnals at high latitude deepen in N216ORCA025 toward the Antarctic shelf break, revealing a lower density than in N96ORCA1. The associated meridional density gradient then drives a strong geostrophic westward shelf break current in N216ORCA025. Validation of the current against mooring observations reveals that in N216ORCA025 it is approximately 50% too strong in the Weddell Sea but in good agreement in the Amundsen Sea, while in N96ORCA1 it is an order of magnitude too weak. The strong shelf break current in the Weddell Sea leads to a counter current through the Drake Passage (Figure 14). The Drake Passage cross-sectional transport depends strongly on the model resolution, with considerable latitudinal structure in N216ORCA025 and a single broad current in N96ORCA1 (Figure 14). The structure in N216ORCA025 is comparable with observations (Koshlyakov et al., 2012; Renault et al., 2011) and related to the mean flow, including the near-coast counter current and standing eddies.

In summary the mean Drake Passage transport for N216ORCA1 is very weak compared to observations and N96ORCA1. However, the meridional section of the transport compares well with observations. The sea ice extent in N216ORCA025 is low due to a warm Southern Ocean and persistent open water convection in the Weddell Sea. In addition, although this model is eddy permitting in the tropics, this is not true at high latitudes and there is no latitude-scaled eddy parameterization (e.g., Gent & McWilliams, 1990). Thus, we have no clear explanation for the weak transport in N216ORCA025.

2.7. AMOC at 26.5°N

The AMOC (as defined by the meridional stream function; a geometrical decomposition of the three-dimensional ocean into two dimensions) comprises the large-scale thermohaline circulation in the Atlantic, which is thought to be an important component of low-frequency climate variability (Park & Latif, 2008; Otterå et al., 2010). In the vicinity of the Atlantic basin, it contributes an important fraction of the

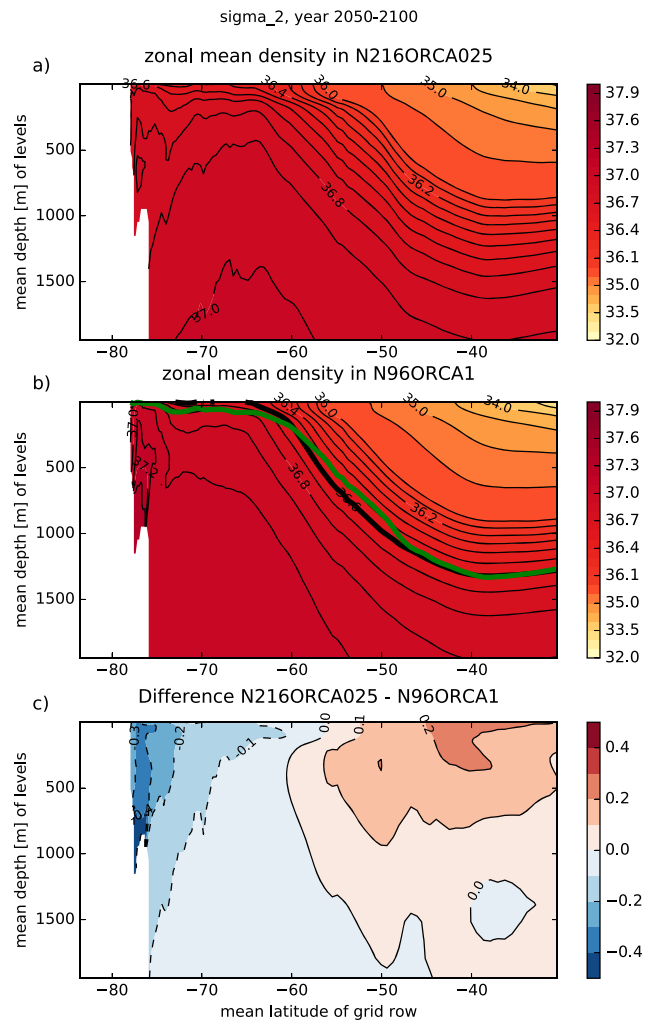


Figure 13. The zonal mean potential density referenced to 2,000-m depth (σ_2) in the upper 2,000 m of the Southern Ocean for N216ORCA025 (a), N96ORCA1 (b), and their difference (c). Bold lines in (b) show the $\sigma_2 = 36.6$ isopycnal for N96ORCA1 (black) and N216ORCA025 (green) to help visualize the flatter isopycnals in N216ORCA025 above approximately 800 m.

poleward heat transport in the coupled atmosphere-ocean system (Trenberth & Caron, 2001) and is thus important to simulate a realistic North Atlantic and global climate.

In the following two sections, we undertake a deeper exploration of the variability in the North Atlantic Ocean in HadGEM3-GC3.1. To attempt to elucidate where resolution may or may not play an important role, we also make use of targeted analyses of the 500-year CMIP6 piControl simulation with the new IPSLCM6 coupled climate model. This uses the same ocean submodel (NEMO) at ORCA1 resolution, importantly also using a shared configuration where differences can be clearly traced. Relevant differences between HadGEM3-GC3.1 and IPSLCM6 in the setup include the employed scheme for turbulent vertical mixing, the choice of the equation of state, and the coupling frequency. IPSLCM6 uses version 6 of the LMDz atmosphere model, which is largely based on Hourdin et al. (2013), at 2.5° zonal and 1.25° meridional resolution with 79 vertical levels. It uses version 3.6 of the LIM sea ice model (Rousset et al., 2014) and the ORCHIDEE land surface model. In this section, this targeted comparison allows us to understand which features in HadGEM3-GC3.1 are more likely due to the ocean resolution and which may be related to model structural differences. We also make comparisons with the ocean analysis product EN4 (Good et al., 2013), which provides gridded (1° × 1°), optimally interpolated observations of temperature and salinity. The interpolation uses fixed decorrelation length scales (two vertical and two horizontal, with larger values near the equator) and relaxes to climatology with an e-folding timescale of 9.5 months.

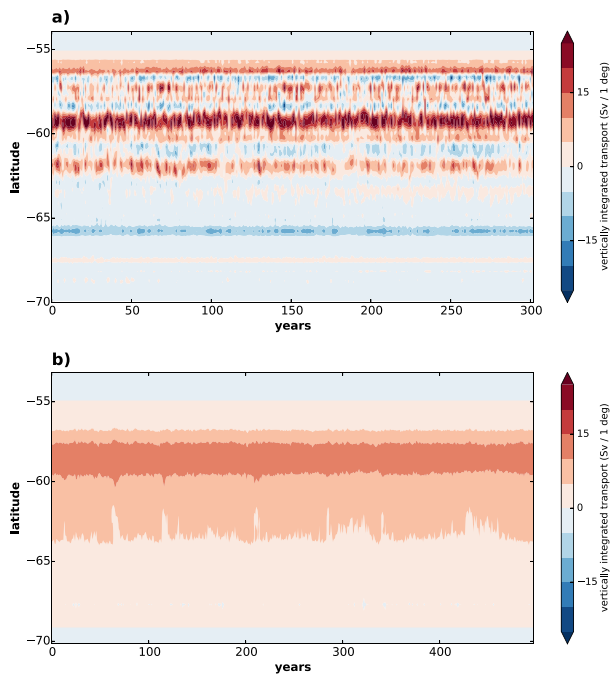


Figure 14. Hovmöller plots of the vertically integrated Drake Passage transport in N216ORCA025 (a) and N96ORCA1 (b). The longitude of the cross section is 68°W.

In this section, we begin by comparing the model simulations with recent instrumental observations at 26.5°N, measured at the RAPID-MOCHA array (Cunningham et al., 2007), used to measure the AMOC. We use the open source *RapidMoc* code (Roberts, 2017) and follow the method of Roberts et al. (2013) to make a fair comparison between models (for which we have full knowledge of the ocean state) and observations (for which we have to make various approximations).

The time mean overturning stream function, at the latitude of the RAPID-MOCHA array, provides a first-order assessment of the three models (Figure 15). For the models, the stream function is constructed in two separate ways, either by using the full model velocities or by using the same combination of local velocity, temperature, salinity, and wind measurements (and assumptions) as in the observations, denoted *RAPID approx*. Observational data are averaged over the period April 2004 to March 2014 inclusive.

It is apparent from these two methodologies that *RAPID approx* produces a closer agreement to the observations (Figure 15). This suggests that previous studies that have compared aspects of the stream function at 26.5°N (such as the depth of the maximum or the depth of the upper cell) against the RAPID-MOCHA array may have been slightly overly pessimistic when using full model velocities. Nonetheless, in all model configurations the strength of the upper cell decreases too rapidly with depth and the depth of the upper cell (defined as where the stream function crosses zero) remains too shallow, occurring around 2,400 m in IPSLCM6, near 2,900 m

in N96ORCA1, and 4,000 m in N216ORCA025, where the observed value is closer to 4,500 m. Within the upper cell, the stream function maximum is also too shallow and too weak though N216ORCA025 is closest with a maximum strength that is within the annual range (estimated as the annual standard deviation) of the observations. Roberts et al. (2018) found a similar improvement in the mean state of the AMOC in the ECMWF climate model when increasing the resolution of the NEMO ocean model from the ORCA1 to ORCA025 configuration. However, it is also important to note that the climate model simulations are designed to be experiencing different external forcings (continuous preindustrial) from the observations. Although the AMOC is expected to weaken under climate change (Collins et al., 2013), it is not clear how it has changed since preindustrial times (Menary et al., 2013).

One systematic difference to note between N216ORCA025 and the ORCA1 models is the depth of the AMOC upper cell (zero crossing). In N216ORCA025, the deeper AMOC upper cell (*RAPID approx*) is suggestive of an AMOC that is dominated by vertical motion/sinking in different regions where the sinking is able to penetrate to deeper depths. Separate work (not shown) suggests N216ORCA025 prefers sinking (vertical motion) in the region of the Grand Banks, whereas in the ORCA1 models this is downstream of the Denmark Straits. The IPSLCM6 stream function is similar to—but overall weaker than—N96ORCA1, consistent with sinking that is in a similar location but that it is more intermittent. Other work has shown that high resolution actually systematically shallows the depth of the AMOC maximum (Deshayes et al., 2013) in model reanalyses at 30°S, opposite to what we show here at 26.5°N. At 26.5°N, a stronger positive relationship between AMOC strength and resolution was seen in targeted experiments using the NEMO ocean model with nested high-resolution grids (Talandier et al., 2014). Here we find that the depth and strength of the AMOC maximum is primarily controlled by model differences, rather than resolution, but that resolution may be important in controlling the full depth of the upper cell. Indeed, the role of resolution (and related parameterizations, such as eddy mixing) may be via determining the depth and locations of the deepest wintertime mixing in the North Atlantic region, in which N216ORCA025 prefers the Labrador Sea (similar to a previous model version; Menary et al., 2015) and the ORCA1 models prefer the Nordic Seas (not shown).

Having shown the depth profile of the AMOC stream function at 26.5°N, it is also instructive to investigate which components of the circulation are contributing to this profile and how these vary with time (Figure 16a). In the observational methodology, the AMOC is the sum of various components (McCarthy et al., 2015), which can also be calculated in the models, though note that the Florida Straits are not separated from the wider

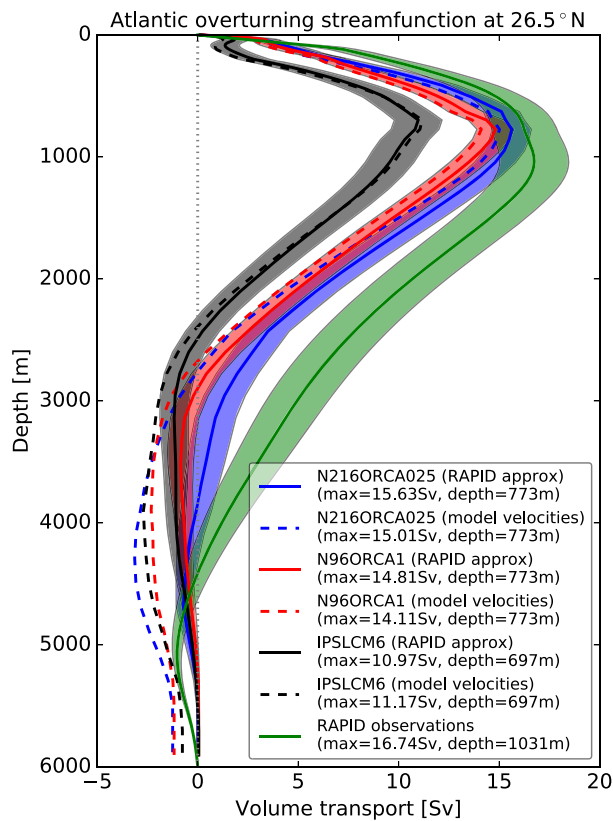


Figure 15. Depth profile of the time mean overturning streamfunction at 26.5°N in models and observations (RAPID-MOCHA, period 2004–2014) calculated using model velocities (dashed) and following the RAPID-MOCHA methodology (solid, shading depicts 1 standard deviation range).

Atlantic Ocean in the ORCA1 models. It can be seen from Figure 16a that, although the total overturning in N216ORCA025 is within the observational annual variability, the various components that contribute this total are not correctly partitioned (albeit with preindustrial forcings). The MOC mean volume transport and percentage difference from observed is 15.6 Sv (–8%) in N216ORCA025, 14.8 Sv (–12%) in N96ORCA1, and 11 Sv (–35%) in IPSLCM6. In all models, the southward upper mid-ocean transport is too strong (around 22–25 Sv, compared to 18 Sv in the observations), which is partly balanced by too strong a Florida Current (34–35 Sv, compared to 31 Sv in the observations). The annual variability in these two flows is comparable or larger than observed (upper mid-ocean: 1.2–1.4 Sv annual standard deviation compared to 1.5 Sv in the observations; Florida Current: 1.4–1.7 Sv compared to 0.7 Sv in the observations), but in all models the annual variability in the total is far too weak (0.9–1.2 Sv compared to 1.7 Sv in the observations), suggesting that there is too much anticorrelation and cancelation of anomalies between the Florida Current and upper mid-ocean. This is likely because the Florida Current is inadequately resolved in all the models. Of the models, the interannual variability in the total AMOC is strongest in IPSLCM6 partly due to strong multidecadal/centennial variability, which does not appear in either resolution of HadGEM3-GC3.1 and cannot be estimated in the observations.

The circulation can be combined with the temperature structure of the Atlantic to provide the heat transport (Figure 16b). Following the RAPID-MOCHA methodology (Johns et al., 2011), we further break down the upper mid-ocean transport into the geostrophic interior and a western boundary wedge. Although the volume transport by the upper mid-ocean is too strong in all models (Figure 16a), the heat transport by the geostrophic interior is of the correct magnitude with similar annual variability. As such, there are clearly compensating temperature biases with the southward flowing water being, on average, too cold (or the northward flowing water in the interior being too warm). In N216ORCA025, the heat

transport by the Florida Current is too strong at 2.79 PW compared to the observed 2.49 PW. In N216ORCA025, the time mean Florida Current heat transport using the observed circulation and model temperatures is 2.45 PW (2.84 PW for the inverse) suggesting that this disparity arises due to the circulation profile and not due to temperature. Note that the good agreement between N96ORCA1/IPSLCM6 and the observations is spurious in the absence of a confined Florida Straits.

The sum of these components provides the total heat transport and, given the methodology we have used, provides a fair estimate of the differences between these models and the RAPID-MOCHA observations. The mean heat transport and percentage difference from observed is 1.05 PW (–14%) in N216ORCA025, 0.90 PW (–26%) in N96ORCA1, and 0.79 PW (–35%) in IPSLCM6. These weak values of ocean heat transport are likely to lead to cold biases in the northern North Atlantic (see section 2.8). In addition, despite strong interannual variability in the model components of the heat transport (especially in N216ORCA025), the variability in the total transport is weak, suggesting too much compensation between components. This might be expected to impact the ability of these simulated oceans to form or maintain large-scale anomalies, thus making them potentially unrealistically overly stable and thus somewhat unsuitable for exploring some aspects of climate variability related to the stability of the AMOC (Jackson et al., 2017; Mecking et al., 2016).

Finally, to link our investigation of volume and heat transports, we show (Figure 17) the relationship between the AMOC volume transport at 1,000 m and the heat transport broken down geometrically into overturning (i.e., contributions from the depth structure) and gyre components (contributions from the zonal structure). The interannual heat transport variability at 26.5°N, in both model and observations, is entirely due to variations in the overturning heat transport, with no relationship between the AMOC and gyre heat transport. The reduction magnitude of the regression slope compared to Johns et al. (2011) and Msadek et al. (2013) is due to the use of annual, rather than monthly, mean data. N216ORCA025 is best able to explore both the high volume transport and high total heat transport values that are seen in the observations.

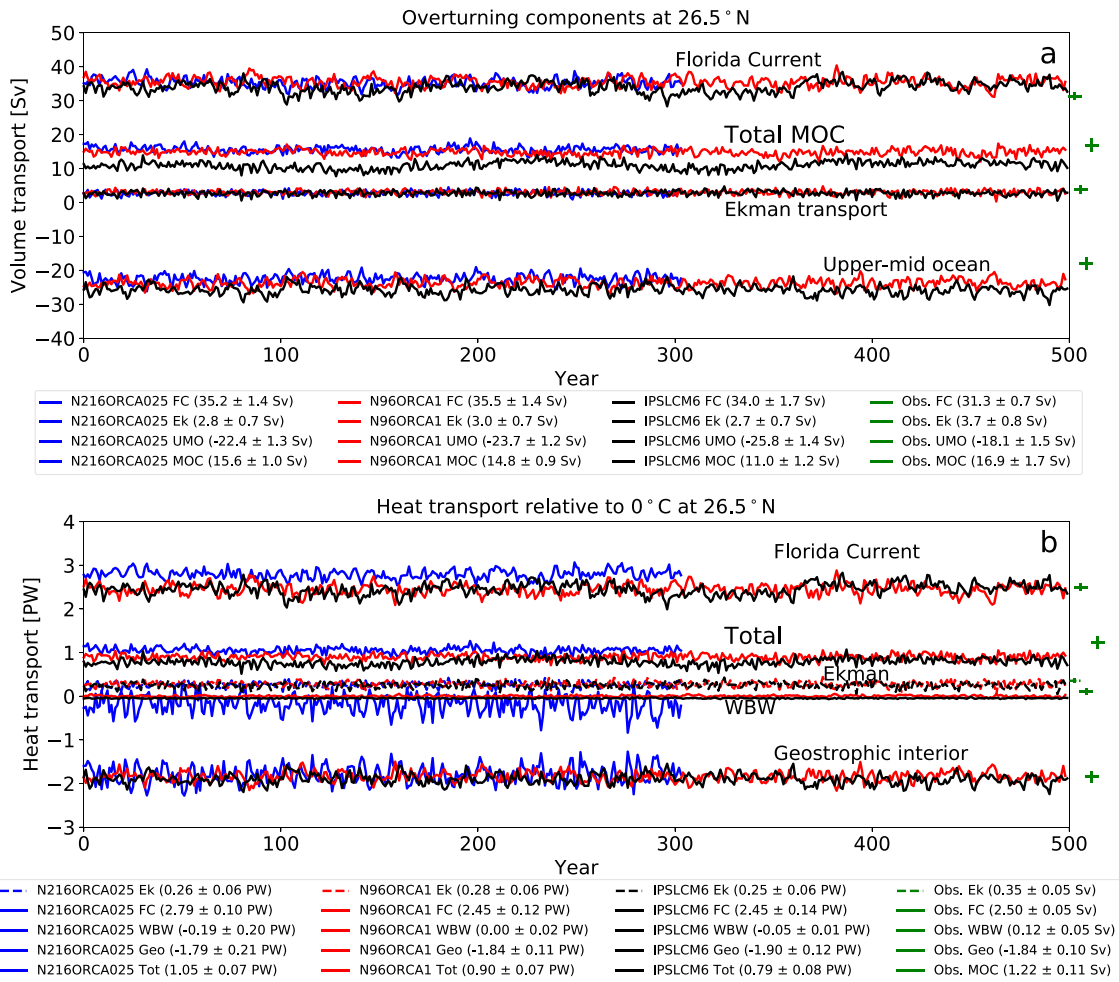


Figure 16. Volume transport components in the three climate models (a), calculated following the RAPID-MOCHA methodology. The time mean and annual standard deviation (vertical whiskers) of the observed volume transport components are shown in green (off axis, right, period 2004–2014). Heat transport components (b), also calculated following the RAPID-MOCHA methodology. The time mean and annual standard deviation (vertical whiskers) of the observed heat transport components are shown in green (off axis, right). Acronyms used are Florida Current (FC), Ekman (Ek), upper mid-ocean (UMO), total volume transport by the meridional overturning circulation (MOC), western boundary wedge (WBW), geostrophic interior (Geo), and total MOC heat transport (Tot).

2.8. The NA SPG

The NA SPG lies between approximately 40° N and the Arctic Ocean, split in two by the Denmark Straits and Iceland-Faroe Ridge that run between Greenland and the north of Scotland. Heat content in the NA SPG has

been shown to be potentially predictable several years in advance (Robson et al., 2012) and itself provides some of the skill in seasonal predictions of other climate variables, such as Atlantic tropical storms (Dunstone et al., 2011). It is a region in which significant, periodic multiannual/decadal timescale variability exists in SSTs or near-surface heat content in both paleorecords (Chylek et al., 2012; Sicre et al., 2008) and in many climate models, although the precise timescales and mechanisms of this variability can be different (Liu, 2012; Menary, Hodson, Robson, Sutton, & Wood, 2015). A detailed analysis of the mechanisms of variability in the NA SPG in these models is beyond the scope of this paper but will be undertaken in future work. Nonetheless, it has previously been shown that the mechanisms of variability in the NA SPG may interact with the mean state (Menary et al., 2015) and so we discuss this next.

In Figure 18 we present the time mean top 500-m depth averaged temperature and salinity in the NA SPG in the ocean reanalysis product EN4 (years

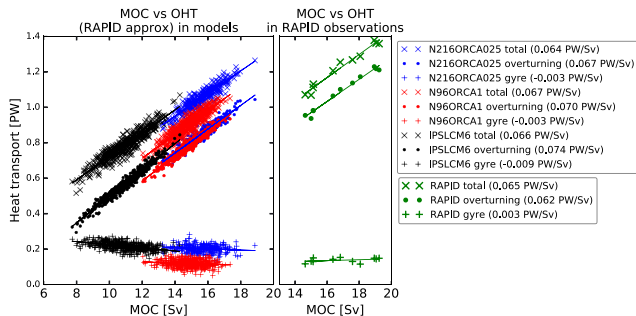


Figure 17. Total meridional overturning circulation versus geometric breakdown of heat transport components in models (left) and observations (2004–2014, right) at 26.5° N. The RAPID-MOCHA methodology is used for calculating the model volume and heat transports. Note the different axis scales; the aspect ratio (PW/Sv) remains the same in both panels.

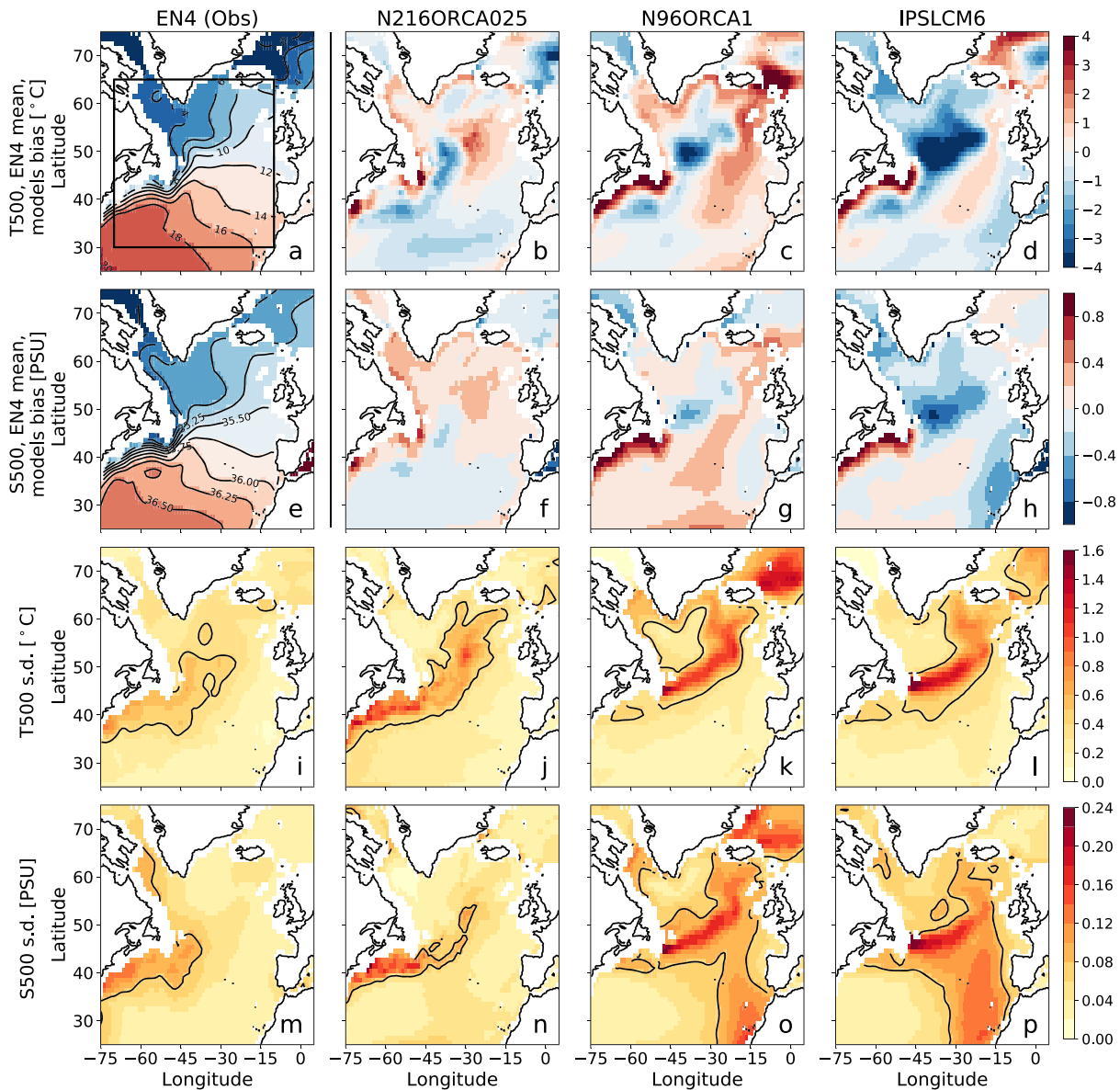


Figure 18. Time mean top 500-m depth averaged temperature (T500, a–d) and salinity (S500, e–h) in EN4 (period 1960–2017, a, e) and biases in N216ORCA025 (b, f), N96ORCA1 (c, g), and IPSLCM6 (d, h). Also shown are the annual standard deviations in T500 (i–l) and S500 (m–p) after applying detrending with a 50-year high-pass filter. Contours are at 0.4 K and 0.08 PSU, respectively. Prior to computing these metrics, all models were regridded to a regular $1 \times 1^\circ$ grid.

1900–2017; Good et al., 2013) and the model biases referenced to the same. As previously noted, this is not a completely like-for-like comparison as, unlike the reanalysis, the preindustrial control simulations are not undergoing forced climate change. However, the patterns of the differences give an indication of where the models may be more or less realistic.

From Figure 18 it can be seen that both the HadGEM3-GC3.1 model versions have a warmer boundary current in the NA SPG than the reanalysis, with the difference particularly large in N96ORCA1. IPSLCM6 does not suffer such a bias, although this is likely due to masking by a global cold bias (not shown). In N216ORCA025, the Gulf Stream appears to separate from the coast at a more realistic latitude than in the ORCA1 models, where a strong dipole in the temperature biases is indicative of a western boundary current that separates too far north. In addition, both the ORCA1 models suggest an overly cool central subpolar gyre, consistent with the well-documented overly zonal nature of the North Atlantic Current (NAC) in low-resolution models (Gnanadesikan et al., 2007). Although IPSLCM6 appears to suffer this deficiency most gravely, this is actually because it is overlaid on to a large-scale cool bias. Thus, in terms of temperature biases over the top 500 m,

N96ORCA1 and IPSLCM6 are similar, with a pattern correlation (after first regridding to a regular $1\times 1^\circ$ grid) over the domain $10-70^\circ\text{W}$, $30-65^\circ\text{N}$ (see box on figure) of $r = 0.74$, whereas the pattern correlation between the HadGEM3-GC3.1 model versions is $r = 0.54$.

In terms of the salinity mean state, the structure of the biases is very similar to the temperature biases, with the ORCA1 models suggesting a Gulf Stream too close to the coast and a NAC that is too zonal. However, one key difference is a relative reduction in magnitude of the NA SPG boundary current region biases in the HadGEM3-GC3.1 model versions and in particular N96ORCA1. Once again, the ORCA1 models are more similar with pattern correlations of $r = 0.84$, compared to $r = 0.19$ for the two HadGEM3-GC3.1 model versions. In the NA SPG as a whole, the general similarity of temperature and salinity biases within each model suggests that ocean circulation (rather than surface forcing) deficiencies, due to the resolution, may contribute a large fraction of the bias.

The interannual variability is assessed via the standard deviation of annual mean depth-averaged temperature and salinity, where both the reanalysis and climate simulations are filtered with a high-pass butterworth filter to remove periods longer than 50 years. This has the effect of removing the secular trend as well as some of the AMV in the observational data (see section 2.4) and any long-term drift in the preindustrial control simulations. In the reanalysis, the remaining signal highlights that the majority of the interannual variability exists on the western side of the basin as the NAC leaves the coast. In reality, snapshots of this current reveal that it is dominated by ocean eddies, which explain why the region of the largest variability (indicated by the contours) has a large horizontal extent (Ducet et al., 2000). In the ORCA1 models, the current here is much more laminar, and thus, the apparent variability is reduced in extent. In N216ORCA025, which permits mesoscale eddies at this latitude, there is increased variance in this region, in better agreement with the reanalysis. Nonetheless, this variability still appears to exist in a band of latitudes that is too narrow. This continues to be the case as the current extends into the center of the NA SPG, where N216ORCA025 indicates high variance along its NAC path and low variance outside, for example, in the Labrador Sea. This is in contrast to the reanalysis, which, at least in terms of temperature, indicates generally similar magnitudes of variance throughout the NA SPG. Note that for salinity, the variance in the northern NA SPG in the reanalysis should be approached with more caution due to a lack of observations (Menary, 2015).

An additional feature in the ORCA1 models (N96ORCA1 and IPSLCM6) is the comparatively large salinity variance in the eastern SPG in the Canary Current region (around 40°N , 20°W). This comma shape is suggestive of leakage of the freshwater signal from the NA SPG. This has also been noted in hosing experiments in the North Atlantic (Swingedouw et al., 2013), where increased leakage was linked with a reduction in the asymmetry between the subtropical and subpolar gyres and associated with a more stable AMOC. Given the importance of the response of the North Atlantic to heat/freshwater forcing in climate projections (Gregory et al., 2005; Stouffer et al., 2006), such a bias should be borne in mind.

3. Summary and Conclusions

In this paper we have presented the preindustrial control (piControl) simulations with HadGEM3-GC3.1 for CMIP6 in N216ORCA025 and N96ORCA1 resolutions. In terms of the key climate phenomena we have specifically reported the following:

- In the equatorial Pacific, the mean SST is improved in N216ORCA025 compared to N96ORCA1, and there are improvements in the westward extent of the pattern of El Niño. Previous work with the ocean component of this model suggests that these improvements are largely related to the increased ocean resolution.
- The model resolutions show similar winter seasonal mean NAO distributions, although N216ORCA025 displays enhanced variance on multidecadal timescales, which is more in line with observed variability.
- In terms of tropical wavenumber-frequency spectra, both model resolutions produce much weaker variability than observed at all scales.
- The propagation characteristics of the MJO and MISO are similar across resolutions, with the northward MISO propagation better represented in general compared to observations.
- The AMV spectra of both resolutions reveal the possibility of long timescale variability in the Atlantic, although with too much variance at shorter timescales. The associated AMV pattern is better represented in N216ORCA025 than in N96ORCA1, likely related to a better representation of the NAC.

Acknowledgments

The climate model simulations are available on the CMIP6 archive (HadGEM3-GC3.1 available Spring 2019; IPSLCM6 data available now). EN4 data are available at <https://www.metoffice.gov.uk/hadobs/en4/>. HadISST data are available at <https://www.metoffice.gov.uk/hadobs/hadisst/>. RAPID-MOCHA data are available at <http://www.rapid.ac.uk/rapidmoc/>. The twentieth Century Reanalysis data are provided by the NOAA/OAR/ESRL PSD, Boulder, Colorado, USA, from their Web site at <https://www.esrl.noaa.gov/psd/>. Support for the Twentieth Century Reanalysis Project data set is provided by the U.S. Department of Energy, Office of Science Innovative and Novel Computational Impact on Theory and Experiment (DOE INCITE) program, Office of Biological and Environmental Research (BER), and by the National Oceanic and Atmospheric Administration Climate Program Office. The IPSL-CM6 experiments were performed using the HPC resources of TGCC under the allocations 2016-A0030107732, 2017-R0040110492, and 2018-R0040110492 (project gencmip6) provided by GENCI (Grand Equipement National de Calcul Intensif). The IPSL-CM6 team of the IPSL climate modeling center (<https://cmc.ipsl.fr>) is acknowledged for having developed, tested, evaluated, tuned the IPSL climate model, as well as performed and published the CMIP6 experiments. This study also benefited from the ESPRI computing and data center (<https://mesocentre.ipsl.fr>) which is supported by CNRS, Sorbonne Université, Ecole Polytechnique, and CNES and through national and international grants. M. B. M., J. Ri., M. B. A., R. E., S. I., C. D. R., R. W., and P. X. were supported by the Joint UK BEIS/Defra Met Office Hadley Centre Climate Programme (GA01101). M. B. M. was additionally supported by the EPICE project funded by the European Union's Horizon 2020 programme, grant agreement 789445. C. D. R. was additionally supported by the PRIMAVERA project funded by the European Union's Horizon 2020 programme, grant agreement 641727. J. Ro was funded by NERC through the DYNAMOC project (NE/M005127/1) and the ACSIS program. T. K. was funded by the National Environmental Research Council (NERC) national capability grant for the U. K. Earth System Modelling project, grant NE/N017951/1, and by the CRESCENDO project funded by the European Union's Horizon 2020 programme, grant agreement 641816. J. D. and J. M. were supported by the French National Programme LEFE/INSU through the DECLIC project. O. B. D.-M. and L. J. G. acknowledge support from NERC through its support of the Oxford

- Stratospheric variability of the polar vortex and the equatorial QBO are well simulated in both N216ORCA025 and N96ORCA1. Both models capture the Holton Tan influence of the QBO on polar vortex strength but with a reduced response amplitude.
- The ACC is far too weak in N216ORCA025 compared to present-day observations and N96ORCA1, which is consistent with results from other climate models coupled to the ORCA025 configuration of the NEMO ocean model (Roberts et al., 2018). In N216ORCA025, this is related to spurious and permanent deep convection in the Weddel Sea.
- The strength of the AMOC at 26.5°N is only slightly weaker than the present-day observed value from RAPID-MOCHA in N26ORCA025 and N96ORCA1 suggesting that boundary conditions (atmosphere/ice sub-models) rather than resolution are most important. Nonetheless, all models suggest a much too shallow upper cell of the AMOC.
- Ocean heat transports at 26.5°N are too weak in all the models. This likely represents a combination of circulation biases (see previous) and temperature biases as the heat transport per unit volume transport is also slightly weaker than observed.
- Both HadGEM3-GC3.1 versions show warm biases in the boundary current regions of the NA SPG. N216ORCA025 and N96ORCA1 are overall warmer and saltier in the NA SPG top 500 m than in IPSLCM6, suggesting that the atmosphere/ice submodels (or common ocean parameterizations) are more important for this aspect of the overall mean state than resolution.
- Within the NAC, in the region of the Grand Banks, N216ORCA025 has similar variability to observed, whereas in N96ORCA1 this variance is located in the central SPG. Comparison with IPSLCM6 suggests that this is related to the resolution.

The westward extent of ENSO, the volume transport by the ACC, the pattern of AMV variability, and the variability in the NAC are examples of important processes affected by the atmosphere/ocean resolution of which the ocean resolution is likely particularly important (Roberts et al., 2018). HadGEM3-GC3.1, at both N216ORCA025 and N96ORCA1 resolution, will be used for many CMIP6 experiments, and these preindustrial control simulations will provide a valuable baseline against which to compare. In general, the model performs adequately in all the metrics we have investigated at either resolution, although the North Atlantic appears to be a region where resolution may be of particular importance. Further work will investigate these aspects in more detail.

References

Adler, R. F., Huffman, G. J., Chang, A., Ferraro, R., Xie, P.-P., Janowiak, J., et al. (2003). The version-2 global precipitation climatology project (GPCP) monthly precipitation analysis (1979–present). *Journal of hydrometeorology*, 4(6), 1147–1167.

Andrews, D. G., Leovy, C. B., & Holton, J. R. (1987). *Middle atmosphere dynamics*. San Diego: Academic press.

Anstey, J. A., & Shepherd, T. G. (2014). High-latitude influence of the quasi-biennial oscillation. *Quarterly Journal of the Royal Meteorological Society*, 140(678), 1–21.

Baldwin, M., Gray, L., Dunkerton, T., Hamilton, K., Haynes, P., Randel, W., et al. (2001). The quasi-biennial oscillation. *Reviews of Geophysics*, 39(2), 179–229.

Barriopedro, D., & Calvo, N. (2014). On the relationship between ENSO, stratospheric sudden warmings, and blocking. *Journal of Climate*, 27(12), 4704–4720.

Behrens, E., Rickard, G., Morgenstern, O., Martin, T., Osprey, A., & Joshi, M. (2016). Southern ocean deep convection in global climate models: A driver for variability of subpolar gyres and Drake Passage transport on decadal timescales. *Journal of Geophysical Research: Oceans*, 121, 3905–3925. <https://doi.org/10.1002/2015JC011286>

Bellenger, H., Guilyardi, É., Leloup, J., Lengaigne, M., & Vialard, J. (2014). ENSO representation in climate models: From CMIP3 to CMIP5. *Climate Dynamics*, 42(7–8), 1999–2018.

Booth, B., Dunstone, N., Halloran, P., Bellouin, N., & Andrews, T. (2012). Aerosols indicated as prime driver of 20th century North Atlantic climate variability. *Nature*, 484(7393), 228–232.

Bracegirdle, T. J., Hyder, P., & Holmes, C. R. (2018b). CMIP5, diversity in southern westerly jet projections related to historical sea ice area: Strong link to strengthening and weak link to shift. *Journal of Climate*, 31(1), 195–211.

Bracegirdle, T. J., Lu, H., Eade, R., & Woollings, T. (2018a). Do CMIP5 models reproduce observed low-frequency North Atlantic jet variability? *Geophysical Research Letters*, 45, 7204–7212. <https://doi.org/10.1029/2018GL078965>

Bryan, F. O., Danabasoglu, G., Nakashiki, N., Yoshida, Y., Kim, D.-H., Tsutsui, J., & Doney, S. C. (2006). Response of the North Atlantic thermohaline circulation and ventilation to increasing carbon dioxide in CCSM3. *Journal of Climate*, 19(11), 2382–2397.

Butler, A. H., Seidel, D. J., Hardiman, S. C., Butchart, N., Birner, T., & Match, A. (2015). Defining sudden stratospheric warmings. *Bulletin of the American Meteorological Society*, 96(11), 1913–1928.

Charlton, A. J., & Polvani, L. M. (2007). A new look at stratospheric sudden warmings. Part I: Climatology and modeling benchmarks. *Journal of Climate*, 20(3), 449–469.

Chylek, P., Folland, C., Frankcombe, L., Dijkstra, H., Lesins, G., & Dubey, M. (2012). Greenland ice core evidence for spatial and temporal variability of the Atlantic multidecadal oscillation. *Geophysical Research Letters*, 39, L0970. <https://doi.org/10.1029/2012GL051241>

Collins, M., Knutti, R., Arblaster, J., Dufresne, J., Fichefet, T., Friedlingstein, P., et al. (2013). Chapter 12: Long-term climate change: Projections, commitments and irreversibility. Climate Change 2013 The Physical Science Basis, Contribution of Working Group I to the Fifth Assessment Report of the Intergovernmental Panel on Climate Change.

Doctoral Training Programme and the National Centre for Atmospheric Sciences (NCAS).

- Compo, G. P., Whitaker, J. S., Sardeshmukh, P. D., Matsui, N., Allan, R. J., Yin, X., et al. (2011). The twentieth century reanalysis project. *Quarterly Journal of the Royal Meteorological Society*, *137*(654), 1–28.
- Cunningham, S., Alderson, S., King, B., & Brandon, M. (2003). Transport and variability of the Antarctic circumpolar current in drake passage. *Journal of Geophysical Research*, *108*(C5), 8084. <https://doi.org/10.1029/2001JC001147>
- Cunningham, S. A., Kanzow, T., Rayner, D., Baringer, M. O., Johns, W. E., Marotzke, J., et al. (2007). Temporal variability of the Atlantic meridional overturning circulation at 26.5°N. *Science*, *317*(5840), 935–938.
- Davini, P., & Cagnazzo, C. (2014). On the misinterpretation of the North Atlantic Oscillation in CMIP5 models. *Climate dynamics*, *43*(5–6), 1497–1511.
- DeMott, C. A., Benedict, J. J., Klingaman, N. P., Woolnough, S. J., & Randall, D. A. (2016). *Diagnosing ocean feedbacks to the MJO: SST-modulated surface fluxes and the moist static energy budget*, vol. 121, pp. 8350–8373. <https://doi.org/10.1002/2016JD025098>
- Dee, D., Uppala, S., Simmons, A., Berrisford, P., Poli, P., Kobayashi, S., et al. (2011). The ERA-Interim reanalysis: Configuration and performance of the data assimilation system. *Quarterly Journal of the royal meteorological society*, *137*(656), 553–597.
- Demory, M.-E., Vidale, P. L., Roberts, M. J., Berrisford, P., Strachan, J., Schiemann, R., & Mizielinski, M. S. (2014). The role of horizontal resolution in simulating drivers of the global hydrological cycle. *Climate dynamics*, *42*(7–8), 2201–2225.
- Deshayes, J., Tréguier, A.-M., Barnier, B., Lecointre, A., Sommer, J. L., Molines, J.-M., et al. (2013). Oceanic hindcast simulations at high resolution suggest that the Atlantic MOC is bistable. *Geophysical Research Letters*, *40*, 3069–3073. <https://doi.org/10.1002/grl.50534>
- Donohue, K., Tracey, K., Watts, D., Chidichimo, M., & Chereskin, T. (2016). Mean Antarctic circumpolar current transport measured in Drake Passage. *Geophysical Research Letters*, *43*, 11,760–11,767. <https://doi.org/10.1002/2016GL070319>
- Ducet, N., Le Traon, P.-Y., & Reverdin, G. (2000). Global high-resolution mapping of ocean circulation from TOPEX/Poseidon and ERS-1 and-2. *Journal of Geophysical Research*, *105*(C8), 19,477–19,498.
- Dunstone, N., Smith, D., & Eade, R. (2011). Multi-year predictability of the tropical Atlantic atmosphere driven by the high latitude North Atlantic ocean. *Geophysical Research Letters*, *38*, L14701. <https://doi.org/10.1029/2011GL047949>
- Essery, R., Best, M., Betts, R., Cox, P. M., & Taylor, C. M. (2003). Explicit representation of subgrid heterogeneity in a GCM land surface scheme. *Journal of Hydrometeorology*, *4*(3), 530–543.
- Eyring, V., Bony, S., Meehl, G. A., Senior, C. A., Stevens, B., Stouffer, R. J., & Taylor, K. E. (2016). Overview of the Coupled Model Intercomparison Project Phase 6 (CMIP6) experimental design and organization. *Geoscientific Model Development*, *9*(5), 1937–1958.
- Garfinkel, C. I., & Hartmann, D. L. (2011). The influence of the quasi-biennial oscillation on the troposphere in winter in a hierarchy of models. Part I: Simplified dry GCMs. *Journal of the Atmospheric Sciences*, *68*(6), 1273–1289.
- Gent, P. R., Large, W. G., & Bryan, F. O. (2001). What sets the mean transport through Drake Passage? *Journal of Geophysical Research*, *106*(C2), 2693–2712.
- Gent, P. R., & McWilliams, J. C. (1990). Isopycnal mixing in ocean circulation models. *Journal of Physical Oceanography*, *20*(1), 150–155.
- Gent, P. R., Yeager, S. G., Neale, R. B., Levis, S., & Bailey, D. A. (2010). Improvements in a half degree atmosphere/land version of the CCSM. *Climate Dynamics*, *34*(6), 819–833.
- Geoffroy, O., Saint-Martin, D., Olivieri, D. J., Voltaire, A., Bellon, G., & Tytécia, S. (2013). Transient climate response in a two-layer energy-balance model. Part I: Analytical solution and parameter calibration using CMIP5 AOGCM experiments. *Journal of Climate*, *26*(6), 1841–1857.
- Gnanadesikan, A., Griffies, S. M., & Samuels, B. L. (2007). Effects in a climate model of slope tapering in neutral physics schemes. *Ocean Modelling*, *16*(1–2), 1–16.
- Goldenberg, S. B., Landsea, C. W., Mestas-Nuñez, A. M., & Gray, W. M. (2001). The recent increase in Atlantic hurricane activity: Causes and implications. *Science*, *293*(5529), 474–479.
- Good, S. A., Martin, M. J., & Rayner, N. A. (2013). EN4: Quality controlled ocean temperature and salinity profiles and monthly objective analyses with uncertainty estimates. *Journal of Geophysical Research: Oceans*, *118*, 6704–6716. <https://doi.org/10.1002/2013JC009067>
- Graham, T. (2014). The importance of eddy permitting model resolution for simulation of the heat budget of tropical instability waves. *Ocean Modelling*, *79*, 21–32.
- Gray, L. J., Anstey, J. A., Kawatani, Y., Lu, H., Osprey, S., & Schenzinger, V. (2018). Surface impacts of the quasi biennial oscillation. *Atmospheric Chemistry and Physics*, *18*(11), 8227.
- Gray, L. J., Beer, J., Geller, M., Haigh, J. D., Lockwood, M., Matthes, K., et al. (2010). Solar influences on climate. *Reviews Of Geophysics*, *48*, RG4001. <https://doi.org/10.1029/2009RG000282>
- Gray, S. T., Graumlich, L. J., Betancourt, J. L., & Pederson, G. T. (2004). A tree-ring based reconstruction of the Atlantic Multidecadal Oscillation since 1567 AD. *Geophysical Research Letters*, *31*, L12205. <https://doi.org/10.1029/2004GL019932>
- Gregory, J., Dixon, K., Stouffer, R., Weaver, A., Driesschaert, E., Eby, M., et al. (2005). A model intercomparison of changes in the Atlantic thermohaline circulation in response to increasing atmospheric CO₂ concentration. *Geophysical Research Letters*, *32*, L12703. <https://doi.org/10.1029/2005GL023209>
- Guilyardi, E. (2006). El niño-mean state-seasonal cycle interactions in a multi-model ensemble. *Climate Dynamics*, *26*(4), 329–348.
- Hamilton, K., Wilson, R. J., & Hemler, R. S. (1999). Middle atmosphere simulated with high vertical and horizontal resolution versions of a GCM: Improvements in the cold pole bias and generation of a QBO-like oscillation in the tropics. *Journal of the atmospheric sciences*, *56*(22), 3829–3846.
- Heuzé, C., Heywood, K. J., Stevens, D. P., & Ridley, J. K. (2013). Southern Ocean, bottom water characteristics in CMIP5 models. *Geophysical Research Letters*, *40*, 1409–1414. <https://doi.org/10.1002/grl.50287>
- Hewitt, H. T., Roberts, M. J., Hyder, P., Graham, T., Rae, J., Belcher, S. E., et al. (2016). The impact of resolving the Rossby radius at mid-latitudes in the ocean: Results from a high-resolution version of the Met Office GC2 coupled model. *Geoscientific Model Development*, *9*(10), 3655–3670.
- Hodson, D. L., & Sutton, R. T. (2012). The impact of resolution on the adjustment and decadal variability of the Atlantic meridional overturning circulation in a coupled climate model. *Climate Dynamics*, *39*(12), 3057–3073.
- Holton, J. R., & Tan, H.-C. (1980). The influence of the equatorial quasi-biennial oscillation on the global circulation at 50 mb. *Journal of the Atmospheric Sciences*, *37*(10), 2200–2208.
- Hourdin, F., Grandpeix, J.-Y., Rio, C., Bony, S., Jam, A., Cheruy, F., et al. (2013). LMDZ5B: The atmospheric component of the IPSL climate model with revisited parameterizations for clouds and convection. *Climate Dynamics*, *40*(9–10), 2193–2222.
- Hurrell, J. W. (1995). Decadal trends in the North Atlantic oscillation: Regional temperatures and precipitation. *Science*, *269*(5224), 676–679.
- Jackson, L., Smith, R. S., & Wood, R. (2017). Ocean and atmosphere feedbacks affecting AMOC hysteresis in a GCM. *Climate Dynamics*, *49*(1–2), 173–191.

- Jiang, X., Waliser, D. E., Xavier, P. K., Petch, J., Klingaman, N. P., Woolnough, S. J., et al. (2015). Vertical structure and physical processes of the Madden-Julian Oscillation: Exploring key model physics in climate simulations. *Journal of Geophysical Research: Atmospheres*, 120, 4718–4748. <https://doi.org/10.1002/2014JD022375>
- Johns, W. E., Baringer, M. O., Beal, L., Cunningham, S., Kanzow, T., Bryden, H. L., et al. (2011). Continuous, array-based estimates of Atlantic ocean heat transport at 26.5N. *Journal of Climate*, 24(10), 2429–2449.
- Jones, P., Jonsson, T., & Wheeler, D. (1997). Extension to the North Atlantic oscillation using early instrumental pressure observations from Gibraltar and south-west Iceland. *International Journal of Climatology: A Journal of the Royal Meteorological Society*, 17(13), 1433–1450.
- Josey, S. A., Kent, E. C., & Taylor, P. K. (1998). *The Southampton Oceanography Centre (SOC) ocean-atmosphere heat, momentum and freshwater flux atlas*. UK: Southampton Oceanography Centre Southampton.
- Kalnay, E., Kanamitsu, M., Kistler, R., Collins, W., Deaven, D., Gandin, L., et al. (1996). The NCEP/NCAR 40-year reanalysis project. *Bulletin of the American meteorological Society*, 77(3), 437–472.
- Kim, D., Xavier, P., Maloney, E., Wheeler, M., Waliser, D., Sperber, K., et al. (2014). Process-oriented MJO simulation diagnostic: Moisture sensitivity of simulated convection. *Journal of Climate*, 27(14), 5379–5395.
- Kim, W. M., Yeager, S., Chang, P., & Danabasoglu, G. (2018). Low-frequency North Atlantic climate variability in the community Earth system model large ensemble. *Journal of Climate*, 31(2), 787–813.
- Klingaman, N., & Woolnough, S. (2014). Using a case-study approach to improve the Madden-Julian oscillation in the Hadley Centre model. *Quarterly Journal of the Royal Meteorological Society*, 140(685), 2491–2505.
- Knight, J. R., Folland, C. K., & Scaife, A. A. (2006). Climate impacts of the Atlantic Multidecadal Oscillation. *Geophysical Research Letters*, 33, L17706. <https://doi.org/10.1029/2006GL026242>
- Koshlyakov, M., Gladyshev, S., Tarakanov, R. Y., & Fedorov, D. (2012). Currents in the drake passage based on the observations in November of 2010. *Oceanology*, 52(3), 299–308.
- Kravtsov, S. (2017). Pronounced differences between observed and CMIP5-simulated multidecadal climate variability in the twentieth century. *Geophysical Research Letters*, 44, 5749–5757. <https://doi.org/10.1002/2017GL074016>
- Kuhlbrodt, T., Jones, C. G., Sellar, A., Storkey, D., Blockley, E., Stringer, M., et al. (2018). The low-resolution version of HadGEM3 GC3.1: Development and evaluation for global climate. *Journal of Advances in Modeling Earth Systems*, 10. <https://doi.org/10.1029/2018MS001370>
- Kuhlbrodt, T., Smith, R. S., Wang, Z., & Gregory, J. M. (2012). The influence of eddy parameterizations on the transport of the Antarctic circumpolar current in coupled climate models. *Ocean Modelling*, 52, 1–8.
- Kunze, M. (2017). Qbo dataserie available at, <http://www.geo.fuberlin.de/en/met/ag/strat/produkte/qbo/index.html>
- Liess, S., & Geller, M. A. (2012). On the relationship between QBO and distribution of tropical deep convection. *Journal of Geophysical Research*, 117, D03108. <https://doi.org/10.1029/2011JD016317>
- Liu, Z. (2012). Dynamics of interdecadal climate variability: A historical perspective. *Journal of Climate*, 25(6), 1963–1995.
- Madden, R. A., & Julian, P. R. (1971). Detection of a 40–50 day oscillation in the zonal wind in the tropical Pacific. *Journal of the Atmospheric Sciences*, 28(5), 702–708.
- Madec, G. (2008). NEMO ocean engine: Note du pole de modélisation, Institut Pierre-Simon Laplace (IPSL), France, No 27 ISSN No 1288-1619. <http://www.nemo-ocean.eu>, Tech. rep., IPSL LSCE, UVSQ, CEA CNRS, Unite Mixte, Bat 712, F-91191 Gif Sur Yvette, France.
- Mann, G., Carslaw, K., Spracklen, D., Ridley, D., Manktelow, P., Chipperfield, M., et al. (2010). Description and evaluation of GLOMAP-mode: A modal global aerosol microphysics model for the UKCA composition-climate model. *Geoscientific Model Development*, 3(2), 519–551.
- Marshall, J., & Radko, T. (2003). Residual-mean solutions for the Antarctic circumpolar current and its associated overturning circulation. *Journal of Physical Oceanography*, 33(11), 2341–2354.
- Marti, O., Braconnot, P., Dufresne, J. L., Bellier, J., Benshila, R., Bony, S., et al. (2010). Key features of the IPSL ocean atmosphere model and its sensitivity to atmospheric resolution. *Climate Dynamics*, 34(1), 1–26.
- Mazloff, M. R. (2012). On the sensitivity of the Drake Passage transport to air-sea momentum flux. *Journal of Climate*, 25(7), 2279–2290.
- McCarthy, G. D., Smeed, D. A., Johns, W. E., Frajka-Williams, E., Moat, B. I., Rayner, D., et al. (2015). Measuring the Atlantic meridional overturning circulation at 26° N. *Progress in Oceanography*, 130, 91–111.
- McInturff, R. M. (1978). Stratospheric warmings, synoptic, dynamic and general-circulation aspects.
- Mecking, J., Drijfhout, S., Jackson, L., & Graham, T. (2016). Stable AMOC off state in an eddy-permitting coupled climate model. *Climate Dynamics*, 47, 2455–2470.
- Meinshausen, M., Vogel, E., Nauels, A., Lorbacher, K., Meinshausen, N., Etheridge, D. M., et al. (2017). Historical greenhouse gas concentrations for climate modelling (CMIP6). *Geoscientific Model Development*, 10, 2057–2116.
- Menary, M. B. (2015). Simulating decadal variability in the North Atlantic Ocean, Ph.D. thesis The University of Reading, Reading, UK.
- Menary, M. B., Hodson, D. L., Robson, J. I., Sutton, R. T., & Wood, R. A. (2015). A mechanism of internal decadal Atlantic ocean variability in a high-resolution coupled climate model. *Journal of Climate*, 28(19), 7764–7785.
- Menary, M. B., Hodson, D. L. R., Robson, J. I., Sutton, R. T., Wood, R. A., & Hunt, J. A. (2015). Exploring the impact of CMIP5 model biases on the simulation of North Atlantic decadal variability. *Geophysical Research Letters*, 42, 5926–5934. <https://doi.org/10.1002/2015GL064360>
- Menary, M. B., Roberts, C. D., Palmer, M. D., Halloran, P. R., Jackson, L., Wood, R. A., et al. (2013). Mechanisms of aerosol-forced AMOC variability in a state of the art climate model. *Journal of Geophysical Research: Oceans*, 118, 2087–2096. <https://doi.org/10.1002/jgrc.20178>
- Mignot, J., Swingedouw, D., Deshayes, J., Marti, O., Talandier, C., Séférian, R., et al. (2013). On the evolution of the oceanic component of the IPSL climate models from CMIP3 to CMIP5: A mean state comparison. *Ocean Modelling*, 72, 167–184.
- Minobe, S., Kuwano-Yoshida, A., Komori, N., Xie, S.-P., & Small, R. J. (2008). Influence of the Gulf Stream on the troposphere. *Nature*, 452(7184), 206–209.
- Msadek, R., Johns, W. E., Yeager, S. G., Danabasoglu, G., Delworth, T. L., & Rosati, A. (2013). The Atlantic meridional heat transport at 26.5°N and its relationship with the MOC in the RAPID array and the GFDL and NCAR coupled models. *Journal of Climate*, 26(12), 4335–4356.
- Myrhe, G., Shindell, D., Bron, F.-M., Collins, W., Fuglesvedt, J., Huang, J., et al. (2013). Chapter 8: Anthropogenic and natural radiative forcing. Climate change 2013, the physical science basis. Contribution of working group I to the fifth assessment report of the intergovernmental panel on climate change.
- Orsi, A. H., Whitworth III, T., & Nowlin Jr, W. D. (1995). On the meridional extent and fronts of the Antarctic circumpolar current. *Deep Sea Research Part I: Oceanographic Research Papers*, 42(5), 641–673.
- Otterå, O. H., Bentsen, M., Drange, H., & Suo, L. (2010). External forcing as a metronome for Atlantic multidecadal variability. *Nature Geoscience*, 3(10), 688–694.
- Park, W., & Latif, M. (2008). Multidecadal and multicentennial variability of the meridional overturning circulation. *Geophysical Research Letters*, 35, L22703. <https://doi.org/10.1029/2008GL035779>

- Rayner, N., Parker, D. E., Horton, E., Folland, C., Alexander, L., Rowell, D., et al. (2003). Global analyses of sea surface temperature, sea ice, and night marine air temperature since the late nineteenth century. *Journal of Geophysical Research*, *108*(D14), 4407. <https://doi.org/10.1029/2002JD002670>
- Renault, A., Provost, C., Sennéchaël, N., Barré, N., & Kartavtseff, A. (2011). Two full-depth velocity sections in the drake passage in 2006 transport estimates. *Deep Sea Research Part II: Topical Studies in Oceanography*, *58*(25-26), 2572–2591.
- Ridley, J. K., Blockley, E. W., Keen, A. B., Rae, J. G., West, A. E., & Schroeder, D. (2018). The sea ice model component of HadGEM3-GC3.1. *Geoscientific Model Development*, *11*(2), 713–723.
- Rienecker, M. M., Suarez, M. J., Gelaro, R., Todling, R., Bacmeister, J., Liu, E., et al. (2011). MERRA: NASA's modern-era retrospective analysis for research and applications. *Journal of climate*, *24*(14), 3624–3648.
- Roberts, C. (2017). Rapidmoc v1., 01, {<https://github.com/cdr30/rapidmoc>}, note <https://doi.org/10.5281/zenodo.1036387>
- Roberts, M. J., Banks, H., Gedney, N., Gregory, J., Hill, R., Mullerworth, S., et al. (2004). Impact of an eddy-permitting ocean resolution on control and climate change simulations with a global coupled GCM. *Journal of Climate*, *17*(1), 3–20.
- Roberts, C. D., Senan, R., Molteni, F., Boussetta, S., Mayer, M., & Keeley, S. (2018). Climate model configurations of the ECMWF integrated forecast system (ECMWF-IFS cycle 43r1) for HighResMIP. *Geoscientific Model Development Discussions*, *2018*, 1–48. <https://doi.org/10.5194/gmd-2018-90>
- Roberts, C., Waters, J., Peterson, K., Palmer, M., McCarthy, G., Frajka-Williams, E., et al. (2013). Atmosphere drives recent interannual variability of the Atlantic meridional overturning circulation at 26.5°N. *Geophysical Research Letters*, *40*, 5164–5170. <https://doi.org/10.1002/grl.50930>
- Robock, A. (2000). Volcanic eruptions and climate. *Reviews of Geophysics*, *38*(2), 191–219.
- Robson, J., Sutton, R., & Smith, D. (2012). Initialized decadal predictions of the rapid warming of the North Atlantic Ocean in the mid 1990s. *Geophysical Research Letters*, *39*, L19713. <https://doi.org/10.1029/2012GL053370>
- Roussenov, V. M., Williams, R. G., Hughes, C. W., & Bingham, R. J. (2008). Boundary wave communication of bottom pressure and overturning changes for the North Atlantic. *Journal of Geophysical Research*, *113*, C08042. <https://doi.org/10.1029/2007JC004501>
- Rousset, C., Vancoppenolle, M., Madec, G., Fichefet, T., Flavoni, S., Barthélemy, A., et al. (2014). The Louvain-La-Neuve sea ice model LIM3.6: Global and regional capabilities. *Geoscientific Model Development*, *8*, 2991–3005.
- Ruti, P. M., Lucarini, V., Dell'Aquila, A., Calmanti, S., & Speranza, A. (2006). Does the subtropical jet catalyze the midlatitude atmospheric regimes? *Geophysical research letters*, *33*, L06814. <https://doi.org/10.1029/2005GL024620>
- Scaife, A., Butchart, N., Warner, C., & Swinbank, R. (2002). Impact of a spectral gravity wave parameterization on the stratosphere in the Met Office Unified Model. *Journal of the atmospheric sciences*, *59*(9), 1473–1489.
- Scaife, A. A., Copestey, D., Gordon, C., Harris, C., Hinton, T., Keeley, S., et al. (2011). Improved Atlantic winter blocking in a climate model. *Geophysical Research Letters*, *38*, L23703. <https://doi.org/10.1029/2011gl049573>
- Schär, C., Vidale, P. L., Lüthi, D., Frei, C., Häberli, C., Liniger, M. A., & Appenzeller, C. (2004). The role of increasing temperature variability in European summer heatwaves. *Nature*, *427*(6972), 332.
- Schlesinger, M. E., & Ramankutty, N. (1994). An oscillation in the global climate system of period 65-70 years. *Nature*, *367*(6465), 723–726.
- Shaffrey, L. C., Stevens, I., Norton, W., Roberts, M., Vidale, P. L., Harle, J., et al. (2009). UK HiGEM: The new UK high-resolution global environment model—Model description and basic evaluation. *Journal of Climate*, *22*(8), 1861–1896.
- Sicre, M.-A., Yiou, P., Eiriksson, J., Ezat, U., Guimbert, E., Dahhaoui, I., et al. (2008). A 4500-year reconstruction of sea surface temperature variability at decadal time-scales off North Iceland. *Quaternary Science Reviews*, *27*(21-22), 2041–2047.
- Simpson, I. R., Blackburn, M., & Haigh, J. D. (2009). The role of eddies in driving the tropospheric response to stratospheric heating perturbations. *Journal of the Atmospheric Sciences*, *66*(5), 1347–1365.
- Spence, P., Saenko, O. A., Sijp, W., & England, M. (2011). The role of bottom pressure torques on the interior pathways of North Atlantic deep water. *Journal of Physical Oceanography*, *42*(1), 110–125.
- Stephenson, D. B., Pavan, V., & Bojariu, R. (2000). Is the North Atlantic oscillation a random walk? *International Journal of Climatology*, *20*(1), 1–18.
- Stouffer, R. J., Yin, J., Gregory, J., Dixon, K., Spelman, M., Hurlin, W., et al. (2006). Investigating the causes of the response of the thermohaline circulation to past and future climate changes. *Journal of Climate*, *19*(8), 1365–1387.
- Sutton, R., & Hodson, D. (2005). Atlantic Ocean forcing of North American and European summer climate. *Science*, *309*(5731), 115–118.
- Swingedouw, D., Rodehacke, C. B., Behrens, E., Menary, M., Olsen, S. M., Gao, Y., et al. (2013). Decadal fingerprints of freshwater discharge around Greenland in a multi-model ensemble. *Climate Dynamics*, *41*(3-4), 695–720.
- Talandier, C., Deshayes, J., Treguier, A.-M., Capet, X., Benschila, R., Debret, L., et al. (2014). Improvements of simulated western north Atlantic current system and impacts on the AMOC. *Ocean Modelling*, *76*, 1–19.
- Thompson, D. W., & Wallace, J. M. (1998). The Arctic oscillation signature in the wintertime geopotential height and temperature fields. *Geophysical research letters*, *25*(9), 1297–1300.
- Timmermann, A., An, S.-I., Kug, J.-S., Jin, F.-F., Cai, W., Capotondi, A., et al. (2018). El Niño–Southern Oscillation complexity. *Nature*, *559*(7715), 535.
- Trenberth, K. E., & Caron, J. M. (2001). Estimates of meridional atmosphere and ocean heat transports. *Journal of Climate*, *14*(16), 3433–3443.
- Trenberth, K. E., & Shea, D. J. (2006). Atlantic hurricanes and natural variability in 2005. *Geophysical Research Letters*, *33*, L12704. <https://doi.org/10.1029/2006GL026894>
- Uppala, S. M., Kållberg, P., Simmons, A., Andrae, U., Bechtold, V., Fiorino, M., et al. (2005). The ERA-40 re-analysis. *Quarterly Journal of the Royal Meteorological Society*, *131*(612), 2961–3012.
- Van Oldenborgh, G. J., Philip, S., & Collins, M. (2005). El Niño in a changing climate: A multi-model study. *Ocean Science*, *1*(2), 81–95.
- Walters, D., Baran, A., Boutle, I., Brooks, M., Earnshaw, P., Edwards, J., et al. (2017). The Met Office Unified Model global atmosphere 7.0/7.1 and JULES global land 7.0 configurations. *Geoscientific Model Development Discussions*, *2017*, 1–78. <https://doi.org/10.5194/gmd-2017-291>
- Walters, D., Boutle, I., Brooks, M., Thomas, M., Stratton, R., Vosper, S., et al. (2017). The Met Office unified model global atmosphere 6.0/6.1 and JULES global land 6.0/6.1 configurations. *Geoscientific Model Development*, *10*(4), 1487.
- Wheeler, M., & Kiladis, G. N. (1999). Convectively coupled equatorial waves: Analysis of clouds and temperature in the wavenumber-frequency domain. *Journal of the Atmospheric Sciences*, *56*(3), 374–399.
- Williams, K., Copestey, D., Blockley, E., Bodas-Salcedo, A., Calvert, D., Comer, R., et al. (2018). The Met Office global coupled model 3.0 and 3.1 (GC3.0 and GC3.1) configurations. *Journal of Advances in Modeling Earth Systems*, *10*(2), 357–380.

- Williams, K. D., Harris, C. M., Bodas-Salcedo, A., Camp, J., Comer, R. E., Copsey, D., et al. (2015). The Met Office Global Coupled model 2.0 (GC2) configuration. *Geoscientific Model Development Discussions*, 8(1), 521–565.
- Xie, P., & Arkin, P. A. (1997). Global precipitation: A 17-year monthly analysis based on gauge observations, satellite estimates, and numerical model outputs. *Bulletin of the American Meteorological Society*, 78(11), 2539–2558.
- Zhang, C. (2005). Madden-Julian Oscillation. *Reviews of Geophysics*, 43, RG2003. <https://doi.org/10.1029/2004RG000158>
- Zhang, R., & Delworth, T. L. (2006). Impact of Atlantic multidecadal oscillations on India/Sahel rainfall and Atlantic hurricanes. *Geophysical Research Letters*, 33, L17712. <https://doi.org/10.1029/2006GL026267>